

$^{238}\text{U}/^{235}\text{U}$ systematics in terrestrial U-bearing minerals

Joe Hiess^{1*}, Daniel J. Condon¹, Noah McLean² and Stephen R. Noble¹

¹ NERC Isotope Geoscience Laboratory, British Geological Survey, Keyworth, Nottinghamshire, NG12 5GG, UK. *Corresponding author - email address: jies@bgs.ac.uk

² Department of Earth, Atmospheric and Planetary Sciences, Massachusetts Institute of Technology, Cambridge, MA 02139, USA.

Manuscript 1215507 accepted for Science Magazine, 13th February 2012.

One sentence summary: $^{238}\text{U}/^{235}\text{U}$ ratios for U-bearing accessory minerals from a diverse suite of terrestrial rocks indicate a >5‰ range with an average zircon value of $^{238}\text{U}/^{235}\text{U} = 137.818 \pm 0.045$ (2σ) which is consistent with the composition of other terrestrial and meteoritic reservoirs.

The present-day $^{238}\text{U}/^{235}\text{U}$ ratio has fundamental implications for U-Pb geochronology and cosmochronology. A value of 137.88 has previously been considered invariant and used without uncertainty to calculate terrestrial mineral ages. We report high-precision $^{238}\text{U}/^{235}\text{U}$ measurements for a suite of U-bearing minerals from 58 samples representing a diverse range of lithologies. This dataset exhibits a >5% range in $^{238}\text{U}/^{235}\text{U}$ that is not clearly related to any petrogenetic, secular or regional trends. Variation between co-magmatic minerals suggests $^{238}\text{U}/^{235}\text{U}$ fractionation processes operate at magmatic temperatures. A mean $^{238}\text{U}/^{235}\text{U}_{\text{zircon}}$ of 137.818 ± 0.045 (2σ), reflects the average uranium isotopic composition and variability of terrestrial zircon. This distribution is broadly representative of the average crustal and ‘bulk Earth’ $^{238}\text{U}/^{235}\text{U}$ composition.

The U-Pb system is widely used as an isotopic chronometer for geological and meteoritic materials that are less than 1 million to greater than 4.5 billion years old. This system is particularly useful because it has two long-lived isotopes, ^{238}U and ^{235}U , which decay at different rates to ^{206}Pb and ^{207}Pb , respectively, permitting the evaluation of closed-system behavior, and because both decay constants have been determined to relatively high precision (1, 2). Daughter isotope determinations from the two decay systems may also be combined to calculate a $^{207}\text{Pb}/^{206}\text{Pb}$ date in concert with an assumed or measured present-day $^{238}\text{U}/^{235}\text{U}$ ratio. With recent advances in sample preparation, isotope ratio mass spectrometry and gravimetric calibration of tracers for isotope dilution methods, the precision of an individual U-Pb or Pb-Pb age determination can exceed 0.1% (2, 3). The U-Pb chronometer has been employed to improve the accuracy of other radio-isotopic systems, such as $^{40}\text{Ar}/^{39}\text{Ar}$ (4), Lu-Hf (5-7), Rb-Sr (8) and Re-Os (9), and to anchor extinct nuclide cosmochronometers utilized to sequence events in the early solar system. Thus, the U-Pb system has far-reaching impacts on the determination of absolute time in geological and meteoric materials.

Due to their high mass, kinetic fractionation of U isotopes was historically expected to be small, and until recently, the present-day $^{238}\text{U}/^{235}\text{U}$ ratio of all natural materials was considered invariant. In geo- and cosmochronology, a $^{238}\text{U}/^{235}\text{U}$ value equal to 137.88 has been used almost exclusively for the past three decades (10) and is based on studies of magmatic and sedimentary uranium ore deposits (11). As published, this presumed invariant ratio and its references cannot be traced back to the International System (SI) of Units (12). More recently, the IUPAC (13) recommend a value of 137.80 from the analysis of six natural ore deposits (14), confirmed by

high-precision isotope ratio analyses using the IRMM 3636 ^{233}U - ^{236}U double spike (15, 16) whose isotopic composition is traceable to SI units. The invariance of the present-day $^{238}\text{U}/^{235}\text{U}$ ratio has been brought into question by studies that have demonstrated U isotopic fractionation in terrestrial materials (17-20). Such fractionation occurs during oxidation-reduction reactions (U^{VI} to/from U^{IV}), coordination change during adsorption, or leaching, and is due to thermodynamic or nuclear field shift effects (21-23). In extraterrestrial materials, excess ^{235}U may result from α -decay of the short-lived ^{247}Cm (24), which has been detected in carbonaceous chondrites and their calcium-aluminum-rich inclusions (25). Recent cosmochronology studies have highlighted the need for coupled $^{238}\text{U}/^{235}\text{U}$ and $^{207}\text{Pb}/^{206}\text{Pb}$ datasets in order to determine accurate ^{207}Pb - ^{206}Pb dates. Thus, it is crucial to re-evaluate (26) the range of natural variation of $^{238}\text{U}/^{235}\text{U}$ in U-bearing minerals commonly analyzed for U-Pb age determinations.

We performed 141 $^{238}\text{U}/^{235}\text{U}$ determinations on a suite of 58 samples of U-bearing accessory minerals that are utilized for U-Pb geochronology (zircon, monazite, apatite, titanite, uraninite, xenotime and baddeleyite), spanning the Quaternary to the Eoarchean and covering a diverse range of igneous and metamorphic petrogenetic settings and geographic locations (27). These data are traceable to SI units because they were measured using a gravimetrically calibrated ^{233}U - ^{236}U tracer (16), measurement uncertainties are on the order of 70 parts per million (ppm) or better.

Our dataset has a $>5.4\%$ range in $^{238}\text{U}/^{235}\text{U}$ (Fig. 1). The lowest measured value is 137.743 from the pegmatite-derived Moacyr monazite, and the highest is 138.490 for the Fish Canyon Tuff titanite, erupted in a large-volume silicic ash flow. Two other samples yield $^{238}\text{U}/^{235}\text{U}$ values greater than 138: BLR-1 titanite (138.068) and Table Cape zircon (138.283). The Miocene Table Cape basanite from Tasmania may be derived from a unique, isotopically heavy reservoir more subtly expressed by Pliocene Bullenmerri (137.862) and Miocene Mornington (137.855) from Victoria, Australia at the higher end of the main zircon $^{238}\text{U}/^{235}\text{U}$ population. These three zircon samples are likely to be mantle-derived and are sourced from regional alkaline volcanic fields. Six monazite samples have $^{238}\text{U}/^{235}\text{U}$ values from 137.743 to 137.856. Most monazite samples are sourced from pegmatites, a lithology with the potential to contain high proportions of low-temperature redox-fractionated protoliths. Resolvable $^{238}\text{U}/^{235}\text{U}$ variation between different accessory phases from the same sample, such as 01RP1 zircon and monazite (65 ppm), Mud Tank zircon and apatite (225 ppm) and Fish Canyon tuff zircon and titanite (4.78%) indicates

crystal-chemical and/or petrogenetic control on $^{238}\text{U}/^{235}\text{U}$ fractionation processes that operate at magmatic temperatures.

Forty-four of forty-five zircon $^{238}\text{U}/^{235}\text{U}$ measurements have a ca. 1‰ range, from 137.772 (Zim265) to 137.908 (168952). There is resolvable variation between samples, but no first-order correlation with age, petrogenetic setting or geographic location. All five samples of uraninite, apatite, xenotime and baddeleyite fall within the compositional range of zircon. The resolvable $^{238}\text{U}/^{235}\text{U}$ differences between samples could arise from multiple processes, including incorporation of uranium from a protolith with fractionated $^{238}\text{U}/^{235}\text{U}$ into parental magma and isotopic fractionation associated with magmatic / mineral crystallization processes. Samples of similar genetic affinity typically show agreement in $^{238}\text{U}/^{235}\text{U}$ values, suggesting isotopic homogenization within some magmatic systems (e.g., zircon from Yellowstone's Lava Creek, Mesa Falls and Huckleberry Ridge ash-flow tuffs; Hungarian volcanic tuffs 97JP32 and 97JP33; Californian tonalites 81P131 and 81P209; Ontarian pegmatites Bancroft and Cardiff; Minnesotan rhyolite and anorthosites MS9930, FC1 and AS3; Greenland tonalites 492118 and 492120; and monazite from British Columbian pegmatites FC-1 and 01RP1).

Of the zircon samples measured, 44 of 45 define an approximately normally distributed population with a mean of 137.818 and standard deviation of 0.022, with population parameters calculated using (28), which corrects for the expected additional dispersion from analytical uncertainties. We propose that this average zircon value and its associated variability ($137.818 \pm 0.045/0.050$, 2σ), which is traceable to the SI system of units, is applicable for the majority of U-Pb determinations and, in the absence of an independently determined $^{238}\text{U}/^{235}\text{U}$, should be adopted for future use in U-Pb geochronology of zircon. The first uncertainty reported reflects the variability found in nature, while the second additionally incorporates systematic uncertainties in the isotopic composition of the tracer. Other phases, such as monazite and titanite require further assessment of their $^{238}\text{U}/^{235}\text{U}$ variability.

Adoption of the average $^{238}\text{U}/^{235}\text{U}_{\text{zircon}}$ value of 137.818 ± 0.045 for use in zircon geochronology will decrease ^{207}Pb - ^{206}Pb , ^{207}Pb - ^{235}U and ^{206}Pb - ^{238}U dates compared to those calculated using the conventional $^{238}\text{U}/^{235}\text{U}$ value of 137.88 (12, 18). For ^{207}Pb - ^{206}Pb dates, the $^{238}\text{U}/^{235}\text{U}$ ratio is implicit in the age equation and the magnitude of the difference is largest, changing gradually from ~1 Myr for <100 Ma samples to ~0.7 Myr at 4 Ga (Fig. 2A). The observed variability in

$^{238}\text{U}/^{235}\text{U}_{\text{zircon}}$ may limit precision for >1 Ga zircon samples with no independent $^{238}\text{U}/^{235}\text{U}$ constraint. For ^{207}Pb - ^{235}U and ^{206}Pb - ^{238}U dates (Fig. 2B,C), the mineral $^{238}\text{U}/^{235}\text{U}$ is used in tracer subtraction and fractionation correction calculations for tracers enriched in ^{235}U that are commonly employed in high-precision U-Pb geochronology (see SOM text). For typical sample/tracer $^{238}\text{U}/^{235}\text{U}$ ratios close to unity, the biases are <500 kyr for $^{207}\text{Pb}/^{235}\text{U}$ dates and <30 kyr for $^{206}\text{Pb}/^{238}\text{U}$ dates <4.4 Ga. For Phanerozoic zircons, the change in $^{206}\text{Pb}/^{238}\text{U}$ dates is <4 kyr.

High-precision U-Pb isotope analyses of closed-system zircon and xenotime have also been exploited to derive a more precise $\lambda^{235}\text{U}$ (2, 3, 29). In this approach, the systematic bias between ^{206}Pb - ^{238}U dates and ^{207}Pb - ^{235}U dates is minimized by solving for a new value of $\lambda^{235}\text{U}$ relative to the more precisely determined $\lambda^{238}\text{U}$ (1). These studies have used an assumed $^{238}\text{U}/^{235}\text{U}$ value equal to 137.88 (2, 3, 29). Mattinson (2) discusses the effects of intermediate daughter disequilibrium, mass isotopic fractionation, tracer calibrations and $^{238}\text{U}/^{235}\text{U}$ on the accuracy and precision of U-Pb analyses. Our dataset includes a subset of samples dated in these previous studies and allows us to better evaluate the impact of a more accurate $^{238}\text{U}/^{235}\text{U}$ on uranium decay constant inter-calibration. Accepting the published U-Pb data (2, 3) and the samples' unique $^{238}\text{U}/^{235}\text{U}_{\text{zircon}}$ values determined in this study yields a recalculated $\lambda^{235}\text{U} = 0.98531 \text{ Gyr}^{-1}$ (Fig. S10) intermediate between the Jaffey et al. (1) counting experiment value and the closed system U-Pb re-evaluations using $^{238}\text{U}/^{235}\text{U} = 137.88$ (2, 3). However, a robust $\lambda^{235}\text{U}$ can only be determined with U-Pb analyses using a tracer calibration that is traceable to SI units and free of other potential sources of bias, so we refrain from suggesting this value be adopted at present and urge caution in abandoning the Jaffey et al (1) $\lambda^{235}\text{U}$ determination until such a dataset has been generated and evaluated.

An emerging $^{238}\text{U}/^{235}\text{U}$ dataset for a wide range of rocks, minerals, and meteorites is now available (17, 18, 25, 30-33) and compiled here (Fig. 3). Given that natural $^{238}\text{U}/^{235}\text{U}$ variation has been demonstrated up to $\sim 0.13\%$ (17, 18) it might be expected that a corresponding variation be observed in the U-bearing mineral data set as $^{238}\text{U}/^{235}\text{U}$ fractionated material from low-temperature environments is incorporated into higher-temperature systems through crustal recycling processes. A first order observation from the compiled $^{238}\text{U}/^{235}\text{U}$ data is that materials formed in near-surface environments (e.g., chemical precipitates) record a wider range compared to crustal rocks and minerals formed in higher-temperature magmatic environments (17, 18). This

suggests that uranium in magmatic and derived crustal reservoirs (e.g., siliciclastic sediments) are isotopically well mixed compared to uranium in materials formed in near-surface environments, and that the low-temperature materials with highly fractionated $^{238}\text{U}/^{235}\text{U}$ comprise volumetrically minor reservoirs that are continually and efficiently homogenized via crustal recycling processes. Second, modern seawater and Quaternary seawater precipitates are systematically lower than the 'bulk Earth' $^{238}\text{U}/^{235}\text{U}$ composition, indicating ^{235}U enrichment in the marine reservoir. Seawater enrichment in ^{234}U (34) by $\sim 147\%$ relative to radioactive secular equilibrium is a well-known consequence of radioactive α -recoil processes and the preferential release of the non-lattice bound ^{234}U daughter nuclide into the hydrological environment (35, 36). Previous studies demonstrated a broad positive correlation between ^{234}U and ^{235}U depletion in near surface environments (17) but a recoil-related mechanism cannot account for $^{235}\text{U}/^{238}\text{U}$ fractionation as both are lattice bound. Zircon acid leaching experiments carried out in this study also recorded a systematic enrichment in ^{235}U in the leachate (27) suggesting preferential leaching of lattice-bound ^{235}U , and similar fractionation has been detected in euxenite leaching experiments (17). By analogy we suggest leaching of lattice bound ^{235}U during long-term chemical weathering of exposed crustal rocks as a viable mechanism to explain ^{235}U enrichment in seawater.

Uranium-bearing accessory minerals from a wide range of crustal and mantle-derived rock types record a restricted (0.07%) range of $^{238}\text{U}/^{235}\text{U}$ values that encompasses nearly all published $^{238}\text{U}/^{235}\text{U}$ values determined on high-temperature (i.e., magmatic) rocks/minerals including granites, dunite and basalts (Fig. 3). The overlap in $^{238}\text{U}/^{235}\text{U}$ values for crust and upper mantle-derived lithologies indicates no resolvable fractionation between the terrestrial reservoirs sampled. Furthermore, notwithstanding $^{238}\text{U}/^{235}\text{U}$ values of meteoritic material recording excess ^{235}U derived from extant ^{247}Cm (24, 25, 37), ordinary chondrites, eucrites and the upper limits for calcium aluminum inclusions and carbonaceous chondrites overlap with the field delineated by terrestrial crust and mantle materials (30, 32, 33). This agreement suggests a uniform $^{238}\text{U}/^{235}\text{U}$ was achieved relatively early during planetary accretion and that high-temperature terrestrial-crust and upper-mantle U isotope compositions are also likely to apply to the lower mantle, therefore defining the bulk silicate Earth isotope composition. In the light of agreement of terrestrial and meteoritic isotope compositions and current Earth accretion models (38), this

average $^{238}\text{U}/^{235}\text{U}$ value of 137.818 ± 0.050 would also represent the isotope composition of ‘bulk Earth’.

References and Notes

1. A. H. Jaffey, K. F. Flynn, L. E. Glendenin, W. C. Bentley, A. M. Essling, *Physics Reviews* **C4**, 1889 (1971).
2. J. M. Mattinson, *Chem Geol* **275**, 186 (2010).
3. B. Schoene, J. L. Crowley, D. J. Condon, M. D. Schmitz, S. A. Bowring, *Geochim Cosmochim Ac* **70**, 426 (2006).
4. P. R. Renne, R. Mundil, G. Balco, K. Min, K. R. Ludwig, *Geochim Cosmochim Ac* **74**, 5349 (2010).
5. E. Scherer, C. Munker, K. Mezger, *Science* **293**, 683 (2001).
6. U. Söderlund, P. J. Patchett, J. D. Vervoort, C. E. Isachsen, *Earth Planet Sc Lett* **219**, 311 (2004).
7. Y. Amelin, *Science* **310**, 839 (2005).
8. O. Nebel, E. E. Scherer, K. Mezger, *Earth Planet Sc Lett* **301**, 1 (2010).
9. D. Selby, R. A. Creaser, K. Dewing, M. Fowler, *Earth Planet Sc Lett* **235**, 1 (2005).
10. R. H. Steiger, E. Jager, *Earth Planet Sc Lett* **36**, 359 (1977).
11. G. A. Cowan, H. H. Adler, *Geochim Cosmochim Ac* **40**, 1487 (1976).
12. D. J. Condon, N. McLean, S. R. Noble, S. A. Bowring, *Geochim Cosmochim Ac* **74**, 7127 (2010).
13. J. R. de Laeter *et al.*, *Pure and Applied Chemistry* **75**, 683 (2003).
14. S. Richter, A. Alonso, W. De Bolle, R. Wellum, P. D. P. Taylor, *International Journal of Mass Spectrometry* **193**, 9 (1999).
15. E. Keegan *et al.*, *Applied Geochemistry* **23**, 765 (2008).
16. S. Richter *et al.*, *International Journal of Mass Spectrometry* **269**, 145 (2008).
17. C. H. Stirling, M. B. Andersen, E. K. Potter, A. N. Halliday, *Earth Planet Sc Lett* **264**, 208 (2007).
18. S. Weyer *et al.*, *Geochim Cosmochim Ac* **72**, 345 (2008).
19. C. J. Bopp, C. C. Lundstrom, T. M. Johnson, J. J. G. Glessner, *Geology* **37**, 611 (2009).
20. G. A. Brennecka, L. E. Wasylenki, J. R. Bargar, S. Weyer, A. D. Anbar, *Environmental Science & Technology* **45**, 1370 (2011).
21. J. Bigeleisen, *Proceedings of the National Academy of Sciences of the United States of America* **93**, 9393 (1996).
22. A. L. Buchachenko, *The Journal of Physical Chemistry A* **105**, 9995 (2001).
23. E. A. Schauble, *Geochim Cosmochim Ac* **71**, 2170 (2007).
24. J. B. Blake, D. N. Schramm, *Nature-Physical Science* **243**, 138 (1973).
25. G. A. Brennecka *et al.*, *Science* **327**, 449 (2010).
26. B. R. Doe, M. F. Newell, *The American Mineralogist* **50**, 613 (1965).
27. Materials and methods are available on Science online.
28. P. Vermeesch, *Chem Geol* **271**, 108 (2010).
29. J. M. Mattinson, *EOS, AGU Fall meeting Supplement Abstract V61A-02*, (2000).
30. Y. Amelin *et al.*, *Earth Planet Sc Lett* **300**, 343 (2010).
31. G. A. Brennecka, L. E. Borg, I. D. Hutcheon, M. A. Sharp, A. D. Anbar, *Earth Planet Sc Lett* **291**, 228 (2010).
32. C. H. Stirling, A. N. Halliday, D. Porcelli, *Geochim Cosmochim Ac* **69**, 1059 (2005).

33. C. H. Stirling, A. N. Halliday, E. K. Potter, M. B. Andersen, B. Zanda, *Earth Planet Sc Lett* **251**, 386 (2006).
34. J. H. Chen, R. Lawrence Edwards, G. J. Wasserburg, *Earth Planet Sc Lett* **80**, 241 (1986).
35. F. Chabaux, J. Riotte, O. Dequincey, *Reviews in Mineralogy and Geochemistry* **52**, 533 (2003).
36. K. Kigoshi, *Science* **173**, 47 (1971).
37. J. B. Blake, T. Lee, D. N. Schramm, *Nature-Physical Science* **242**, 98 (1973).
38. J. F. Rudge, T. Kleine, B. Bourdon, *Nature Geosci* **3**, 439 (2010).
39. A. Bouvier, L. J. Spivak-Birndorf, G. A. Brennecka, M. Wadhwa, *Geochim Cosmochim Ac* **75**, 5310 (2011).
40. C. Montoya-Pino *et al.*, *Geology* **38**, 315 (2010).
41. G. A. Brennecka, A. D. Herrmann, T. J. Algeo, A. D. Anbar, *Proceedings of the National Academy of Sciences* **108**, 17631 (2011).
42. J. M. Mattinson, *Chem Geol* **220**, 47 (2005).
43. T. E. Krogh, *Geochim Cosmochim Ac* **37**, 485 (1973).
44. W. A. Russell, D. A. Papanastassiou, T. A. Tombrello, *Geochim Cosmochim Ac* **42**, 1075 (1978).
45. F. Albarède *et al.*, *Geochim Cosmochim Ac* **68**, 2725 (2004).
46. C.-C. Shen *et al.*, *Chem Geol* **185**, 165 (2002).
47. J. H. Chen, R. L. Edwards, G. J. Wasserburg, in *Uranium-Series Disequilibrium: Applications to Earth, Marine and Environmental Sciences*, M. Ivanovich, R. S. Harmon, Eds. (Clarendon Press, Oxford, 1992), pp. 174-206.
48. M. Thirlwall, *Journal of Analytical Atomic Spectrometry* **16**, 1121 (2001).
49. P. Deschamps, R. Doucelance, B. Ghaleb, J.-L. Michelot, *Chem Geol* **201**, 141 (2003).
50. D. J. Condon *et al.*, in *Geological Society of America Annual Meeting*. (2010), vol. 42, pp. 657.
51. S. Richter *et al.*, *International Journal of Mass Spectrometry* **295**, 94 (2010).
52. H. Cheng *et al.*, *Chem Geol* **169**, 17 (2000).
53. D. W. Davis, T. E. Krogh, *Chem Geol* **172**, 41 (2001).
54. N. McLean, J. Bowring, S. Bowring, *Geochemistry Geophysics Geosystems*, (2011).
55. Contact Dan Condon (dcondon@bgs.ac.uk) for data.
56. M. A. Lanphere, D. E. Champion, R. L. Christiansen, G. A. Izett, J. D. Obradovich, *Geol Soc Am Bull* **114**, 559 (2002).
57. J. A. Chambers *et al.*, *Journal of the Geological Society* **165**, 725 (2008).
58. M. D. Schmitz, S. A. Bowring, *Geochim Cosmochim Ac* **65**, 2571 (2001).
59. F. W. McDowell, W. C. McIntosh, K. A. Farley, *Chem Geol* **214**, 249 (2005).
60. R. R. Parrish, *Can J Earth Sci* **27**, 1431 (1990).
61. M. Ganerød *et al.*, *Chem Geol* **286**, 222 (2011).
62. M. S. A. Horstwood, G. L. Foster, R. R. Parrish, S. R. Noble, G. M. Nowell, *Journal of Analytical Atomic Spectrometry* **18**, 837 (2003).
63. J. Palfy, R. R. Parrish, K. David, A. Voros, *Journal of the Geological Society* **160**, 271 (2003).
64. J. Sláma *et al.*, *Chem Geol* **249**, 1 (2008).
65. A. A. Monaghan, R. R. Parrish, *Journal of the Geological Society* **163**, 15 (2006).
66. P. W. Haines, M. Hand, M. Sandiford, *Australian Journal of Earth Sciences* **48**, 911 (2001).
67. J. C. Neilson, B. P. Kokelaar, Q. G. Crowley, *Journal of the Geological Society* **166**, 545 (2009).

68. J. N. Aleinikoff *et al.*, *Geol Soc Am Bull* **118**, 39 (2006).
69. D. Gasquet *et al.*, *Bulletin de la Societe Geologique de France* **181**, 227 (2010).
70. S. E. Jackson, N. J. Pearson, W. L. Griffin, E. A. Belousova, *Chem Geol* **211**, 47 (2004).
71. E. S. Larsen, C. L. Waring, J. Berman, *American Mineralogist* **38**, 1118 (1953).
72. L. P. Black, B. L. Gulson, *BMR Journal of Australian Geology and Geophysics* **3**, 227 (1978).
73. J. N. Aleinikoff *et al.*, *Am J Sci* **307**, 63 (2007).
74. L. Corriveau, L. M. Heaman, F. Marcantonio, O. Breemen, *Contrib Mineral Petr* **105**, 473 (1990).
75. G. R. Tilton *et al.*, *Bulletin of the Geological Society of America* **66**, 1131 (1955).
76. C. L. Kirkland *et al.*, *Precambrian Res* **187**, 223 (2011).
77. R. R. Parrish, S. R. Noble, *Reviews in Mineralogy and Geochemistry* **53**, 183 (2003).
78. D. R. Nelson, “168952: biotite-hornblende tonalite, Salt Well” (Western Australia Geological Survey, 2001).
79. L. M. Heaman, *Chem Geol* **261**, 43 (2009).
80. R. A. Stern, S. Bodorkos, S. L. Kamo, A. H. Hickman, F. Corfu, *Geostandards and Geoanalytical Research* **33**, 145 (2009).
81. K. Horie, A. P. Nutman, C. R. L. Friend, H. Hidaka, *Precambrian Res* **183**, 25 (2010).
82. J. Hiess, V. C. Bennett, A. P. Nutman, I. S. Williams, *Geochim Cosmochim Acta* **73**, 4489 (2009).

Acknowledgements. We acknowledge NERC funding (Fellowship NE/C517909/1, NIGFSC award IP/1028/0508 and recurrent support to NIGL), funding from the European Community’s Seventh Framework Programme (FP7/2007-2013) grant agreement No. [215458] and NSF Award EAR 0451802 (the EARTHTIME project). We thank N. Atkinson, M. Horstwood and N. Roberts for assistance in the laboratory; J. Aleinikoff, J. Boyce, D. Chew, P. Fitzgerald, D. Kimbrough, C. Kirkland, J. Mattinson, R. Parrish, P. Renne, N. Reyner, G. Rossmann, M. Schmitz, K. Sircombe, M. Wingate and J. Woodhead for provision of samples; GEUS for permission to publish on 492118/20; S. Bowring, R. Parrish, B. Schoene, M. Schmitz, J. Mattinson and others for discussions and three reviewers for helpful comments. All data are available in the Supporting Online Material.

Supporting Online Material

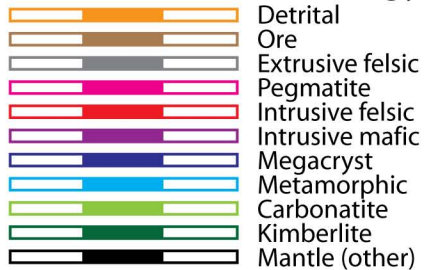
www.sciencemag.org
 Materials and Methods
 Supporting online text
 Figs. S1-S10
 Tables. S1-S6
 References (42-82)
 Databases S1-S5

Fig. 1. (A) $^{238}\text{U}/^{235}\text{U}$ mineral summary plot including the 44 samples used to define our recommended zircon composition represented by the yellow band. Solid and open boxes for each sample represent 2σ measured and total uncertainties respectively. (B) Insert including one zircon and two titanite samples omitted from (A) highlighting the total range of sample compositions observed. Sample solid boxes represent 2σ total uncertainties.

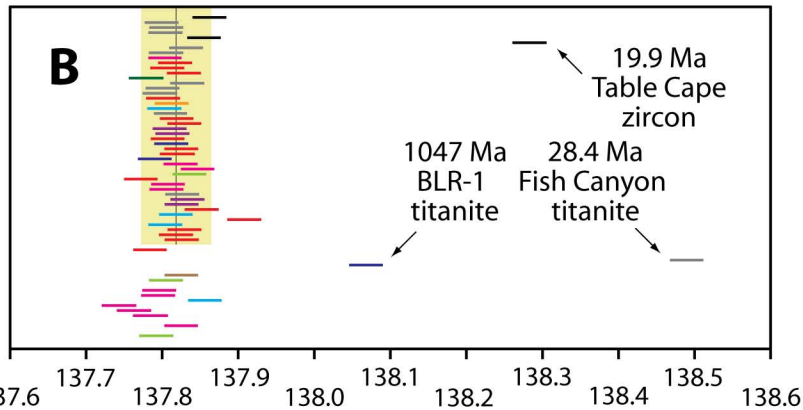
Fig. 2. Plot of absolute differences between zircon (A) ^{207}Pb - ^{206}Pb , (B) ^{207}Pb - ^{235}U and (C) ^{206}Pb - ^{238}U dates calculated with the consensus $^{238}\text{U}/^{235}\text{U}$ of 137.88 and the newly defined value of 137.818 ± 0.045 . Gray bands represent the 2σ uncertainty from the variability in zircon $^{238}\text{U}/^{235}\text{U}$ determined in this study. The difference is calculated by subtracting the Pb-Pb or U-Pb date calculated using $^{238}\text{U}/^{235}\text{U} = 137.818 \pm 0.045$ from the Pb-Pb or U-Pb date calculated using $^{238}\text{U}/^{235}\text{U}$ of 137.88. U-Pb dates are modeled using typical analytical parameters (sample/tracer $^{238}\text{U}/^{235}\text{U} = 1$) to illustrate the magnitude of differences.

Fig. 3. Compilation of $^{238}\text{U}/^{235}\text{U}$ data obtained on a wide variety of geological and extra-terrestrial materials. The ‘Bulk Earth’ field (yellow band) is based upon the terrestrial/high-temperature dataset, consistent with eucrites and ordinary chondrites. Seawater and related precipitates show a systematic enrichment in ^{235}U compared to the ‘Bulk Earth’ field. Data are from literature sources (17, 18, 25, 30-33, 39-41) and this study (zircon and other U-bearing minerals).

Lithology



$^{238}\text{U}/^{235}\text{U}$



Age (Ma) Sample

0.2	Bullenmerri
0.6	Lava Creek
1.3	Mesa Falls
2.1	Huckleberry
14.7	Mornington
28.5	Fish Canyon
61.3	Tardee
63.4	01RP1
65.9	BBC-48
79.6	88-WV-100
90.2	VL-9
95.2	Koffiefontein
238.7	Litre
240.5	97JP33
241.2	97JP32
275.9	49069
317.9	Mag Stream
337.1	Plešovice
343.4	ASW124
404.0	Shap
414.9	Etive
418.4	Temora-2
420.5	R33
493.5	R22563
524.4	M127
559.7	81P-131
560.7	81P-209
574.0	RC140/1
608.5	GJ-1
635.0	Larsen
732.0	Mud Tank
850.0	Zim265
1060	Bancroft
1090	Cardiff
1096	MS99-30
1098	FC1
1098	AS3
1665	194720
1820	Sugluk Sand
2002	168952
2500	PCA-M2438-90
3467	OG1
3850	492118
3880	492120

A

$^{238}\text{U}/^{235}\text{U}_{\text{zircon}}$
 137.818 ± 0.045
 (2 σ uncertainty)

Zircon

19.9 $\Delta 33$

Uraninite

31.4 Durango
349.0 Mud Tank

Apatite

54.3 FC-1
63.4 01RP1
424.9 44069
504.3 Moacyr
510.0 Stern
1876 91-HSA-47

Monazite

999.7 z6413

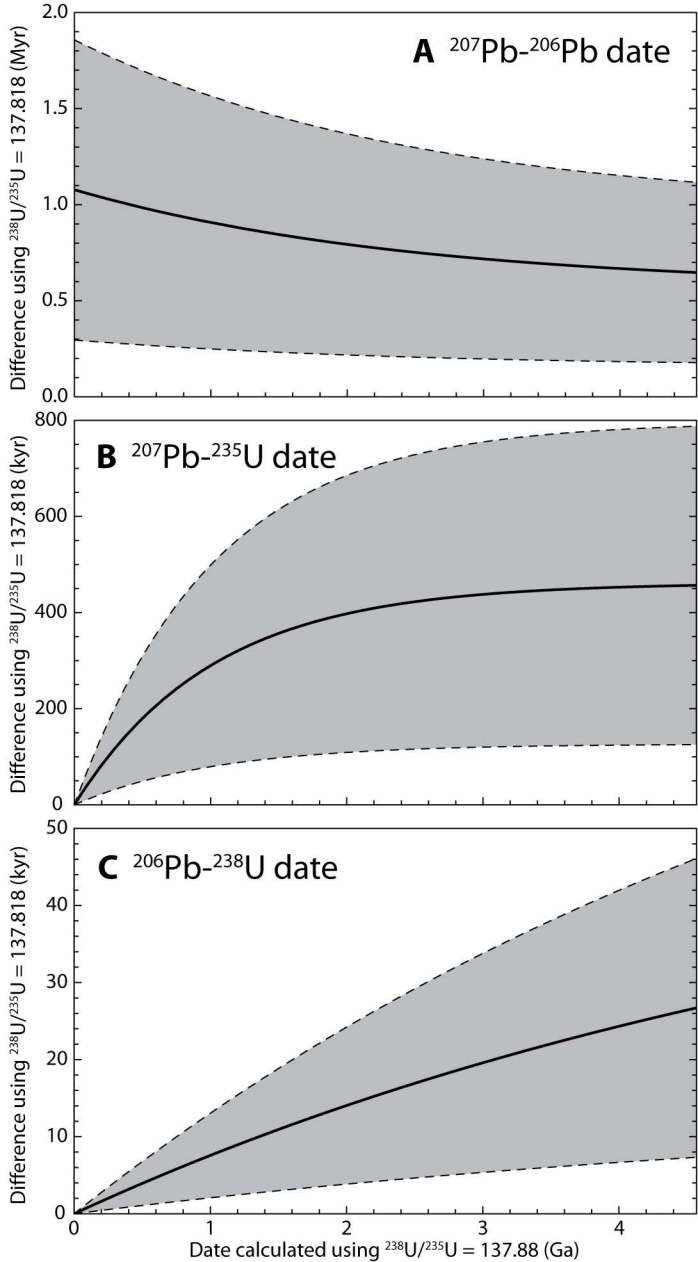
Xenotime

2059 Phalaborwa

Baddeleyite

137.68 137.72 137.76 137.80 137.84 137.88 137.92

$^{238}\text{U}/^{235}\text{U}$



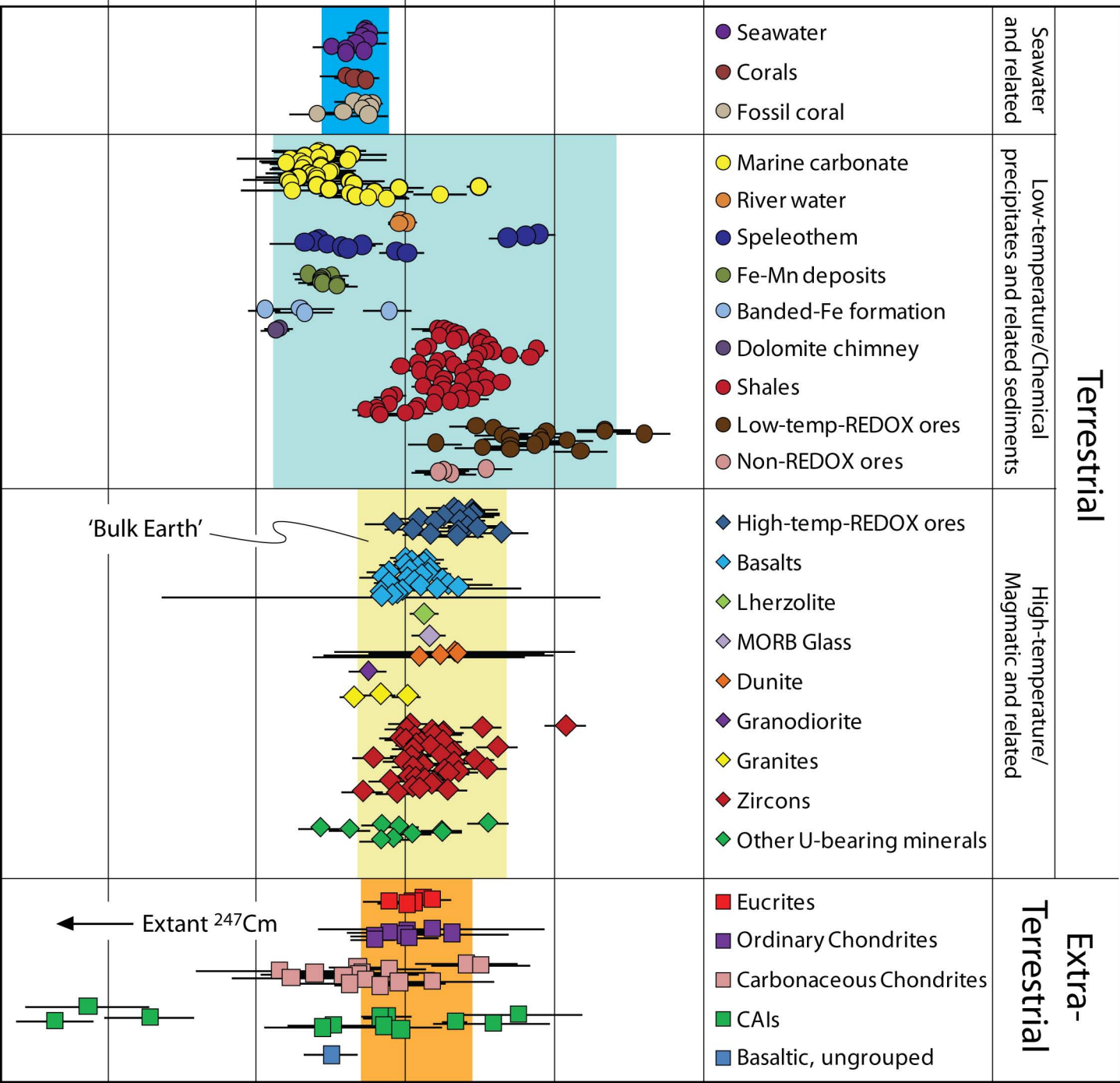
137.6

137.7

137.8

137.9

138.0

 $^{238}\text{U}/^{235}\text{U}$ 



Supporting Online Material for

$^{238}\text{U}/^{235}\text{U}$ systematics in terrestrial U-bearing minerals

Joe Hiess, Daniel J. Condon, Noah McLean and Stephen R. Noble

correspondence to: jies@bgs.ac.uk

This PDF file includes:

Materials and Methods
SOM Text
Figs. S1 to S10
Tables S1 to S6

Other Supporting Online Material for this manuscript includes the following:

Databases S1 to S5 as zipped archives:

Database_S1._TIMSall
Database_S2._MC-ICPMSstds
Database_S3._MC-ICPMSzircon
Database_S4._MC-ICPMSotherminerals.leachates
Database_S5._Compilation

Materials and Methods

S1. Sample descriptions

The minerals analysed were sourced from lithologies representing a broad range of geological environments and processes, covering a wide range of ages and geographic distribution (Figure S1; Table S1). Source rocks ranged from detrital sediments, ore deposits, felsic volcanics, pegmatites, granitoid, intermediate and mafic plutonics (including ophiolite sections), megacrysts, high-grade metamorphic rocks, and unambiguously mantle-derived rocks including carbonatites and kimberlites. Zircon was recovered from all source lithologies while other U-bearing minerals that are commonly used in U-Pb geochronology, including titanite, monazite, apatite, xenotime, uraninite and baddeleyite, were also targeted from a subset of suitable lithologies. Three samples included two co-existing uranium-bearing minerals: zircon-titanite (Fish Canyon Tuff), zircon-monazite (01RP1 pegmatite) and zircon-apatite (Mud Tank carbonatite).

S2. Sample dissolution and purification

High-purity mineral aliquots were concentrated using conventional mineral separation techniques. Multi-grain fractions and megacryst fragments were processed for each sample to yield sufficient purified U for the high-precision $^{238}\text{U}/^{235}\text{U}$ determinations. Therefore, these analyses, excluding those made on single fragments of large megacrysts, reflect volume and concentration-weighted average values. For several samples, additional aliquots (batches) of the same mineral separate were processed to check the reproducibility of our dissolution and purification steps.

Zircon preparation broadly followed the chemical abrasion pre-treatment method (42). The annealing and leaching pre-treatment was performed on zircons to ensure that $^{238}\text{U}/^{235}\text{U}$ determinations were obtained on the closed-system zircon utilized in U-Pb geochronology studies. This pre-treatment also ensures that mineral or melt inclusions that are potentially not closed systems and possibly possess U isotope compositions different from the host zircons were removed. Multi-grain fractions and megacryst fragments were transferred into quartz dishes and annealed in a muffle furnace at 900°C for 60 hrs. The minerals were then weighed and transferred into pre-cleaned, Savillex PFA beakers. Zircon was leached in 29N HF for 12 hrs at 180°C in a Parr pressure vessel. Zircon leachates were stored separately in pre-cleaned Savillex beakers, and the residual grains were fully dissolved in 29N HF for >48 hours at 240°C in Savillex PFA microcapsules housed within a 125 ml Parr pressure vessel. Following dissolution, samples were dried to fluorides then re-dissolved in 11N HCl at 180°C over 12 hrs. This process was repeated until total sample dissolution and conversion to chloride form was achieved and verified by inspection under an optical microscope.

The dissolution of other silicate minerals (titanite, baddeleyite) followed the 29N HF and 11N HCl steps used for residual zircon. Phosphates (monazite, apatite and xenotime) were dissolved in 6N HCl; uraninite was dissolved in 16N HNO₃. Solutions of minerals other than zircon represent the bulk dissolution of an entire non-annealed phase; the only exception to this was a single leachate that was separated from batch 2 of the Fish Canyon Tuff titanite. The IRMM 3636 ^{233}U - ^{236}U tracer (16) was added and equilibrated with the samples after dissolution was complete, but prior to anion exchange chemistry procedures. Uranium was chemically separated from the mineral matrix solutions using HCl-based anion-exchange chromatography with AG-1 X8 resin (43).

For silicate minerals, the HF dissolution and chloride conversion steps removed virtually all Si matrix as volatile SiF₄. The remaining principal matrix elements form cationic species in ≥6M HCl (Zr, Hf, REE, Ca) and are strongly excluded from binding to the anion exchange resin. As a consequence, matrix was strongly separated from U, which is strongly adsorbed to the resin as an anionic complex (43). The relatively small Th partition coefficient in 3M HCl on AG-1 X8 anion resin results in most Th being separated from U during initial elution of the cationic matrix species. Residual Th on the column following matrix elution was incorporated into the U fraction during stripping of U from the resin. This Th was monitored as during MC-ICPMS analysis. Correction of the U isotope spectra for Th, manifested as ²³²ThH⁺ interference on ²³³U, was based on a ²³²Th measurement during static U isotope data collection together with a daily quantification of hydride production. Experimental evaluation of Th and U hydride production during typical optimized tuning conditions of the Neptune MC-ICPMS showed that ²³²ThH⁺ and ²³⁸UH⁺ production rates were equivalent. A daily ²³⁸UH⁺ production value, obtained by measurement of CRM 112a at the start of each analytical session following tuning of the MC-ICPMS, was therefore adequate for constraining the ²³²ThH⁺ production rate. Over several days of continuous operation, hydride production was observed to decrease slightly but was stable and consistent on timescales of a typical <24 hr analytical session. Hydride production ranged from ~2.7 to ~1.0 ppm during the course of the study, with an average hydride production rate of ~2 ppm. Measured zircon ²³²Th/²³³U ranged from 0.0002 to 0.2 with an average of 0.03. The average resulting ²³²ThH⁺/²³³U was 6 × 10⁻⁸, corresponding to an insignificant correction on the ²³³U peak and an insignificant average change of 0.06 ppm to the ²³³U/²³⁶U ratio used for mass bias correction (corrections ranged from a minimum 0.0004 ppm to a maximum 0.5 ppm).

S3. IRMM 3636 ²³³U-²³⁶U double spike

The IRMM 3636 mixed ²³³U-²³⁶U double spike (16) was employed to accurately correct for mass fraction during sample processing and isotope ratio analyses. The ²³³U/²³⁶U ratio of this tracer has been calibrated using gravimetric principles, and its value is therefore traceable to SI units. We have corrected the sample ²³⁸U/²³⁵U for minor contributions of ²³⁵U and ²³⁸U from the IRMM 3636 tracer, and adjusted the ²³³U/²³⁶U ratio of the spike to account for the decay of ²³³U (half life = 159,200 years) during the time elapsed between the date of determination of the molar abundances used for the ²³³U/²³⁶U ratio (16) and the date of our measurements. Uranium concentrations of samples were determined on a small aliquot, and then sample-spike solutions were mixed to give a ²³⁸U/²³⁶U ratio of 25-120 to minimize tailing of ²³⁶U onto ²³⁵U due to ion scattering (16).

S4. Mass Spectrometry and Data Reduction

Uranium isotopic ratios were measured on the Thermo-Electron Triton multi-collector thermal ionization mass spectrometer (TIMS) and Thermo Fisher Scientific Neptune plus multi-collector inductively coupled plasma mass spectrometer (MC-ICPMS) at the NERC Isotope Geoscience Laboratory (NIGL), UK. Analyses were performed on two analytical platforms because (1) the NIGL Neptune MC-ICPMS was purchased, installed and commissioned after the initiation of the project, (2) the ICPMS permitted analysis of the smaller U samples in this study due to its higher sensitivity for U compared to TIMS, and (3) analyses of the same mineral on both platforms provides an additional opportunity to assess and quantify external reproducibility.

S4.1. Method Configuration and Running Conditions: TIMS

Triton TIMS analyses were made following the methods outlined in (12). Samples were loaded onto zone refined Re double filaments in dilute (2%) HNO₃ and slowly dried down before in-run

evaporation at 1.8 – 2.4A, and ionization at 4.6 – 5.4A. Isotopes were analysed as U^+ ions on five Faraday collectors (Table S2A) with $10^{11} \Omega$ resistors following repeated amplifier gain calibrations. Amplifier response times verified that <10 ppm residuals are achieved within 2-3 seconds and ion beam intensities were safely recovered after >3 second magnet settling times. To accommodate the limits of the Faraday detector system, 12 - 44V ^{238}U and 0.09 - 0.32V ^{235}U signal intensities provided sufficient counting statistics while avoiding amplifier saturation.

S4.2. Method Configuration and Running Conditions: MC-ICPMS

Neptune-plus MC-ICPMS analyses were conducted between January and May 2011. The mass spectrometer was coupled to either an Aridus I or II desolvating nebulizer (CETAC Technologies) that introduced the ~ 115 ppb U solutions at $80 \mu L/\text{minute}$, consuming $\sim 1 \mu g$ of U per analysis or $1/10^{\text{th}}$ the mass required for a TIMS analysis. Sensitivity under these conditions was $\sim 350V / \text{ppm U}$, consistently providing $\sim 40V$ ^{238}U . Ar and N_2 flow rates and zoom optics were tuned daily for optimum sensitivity. Although amplifier gains were stable over week-long timescales, they were measured every day prior to data acquisition. Amplifier response times were also monitored daily to ensure they conformed to the same standards as TIMS analyses. All intensities were measured on Faraday collectors with $10^{11} \Omega$ resistors (Table S2B). A single analysis involved three separate methods. The first and third method were identical and involved simultaneous determinations of “half-masses” at 232.54, 233.54, 234.54, 235.54, 236.54, 237.54 and 238.54 u using the L3 to H3 collectors. The second method occurred between the first and third, and was a measurement of the “on-mass” peaks of ^{232}Th , ^{233}U , ^{234}U , ^{235}U , ^{236}U , 237.04 u and ^{238}U using the L3 to H3 collectors. Each method began with either a single (method 1 and 3) or duplicate (method 2) peak-centering scan(s), followed by a 30 second wait before a 63 second defocused electronic baseline measurement. Each method consisted of 105 measurement cycles, broken into seven blocks of 15 cycles to ensure complete amplifier rotation was accomplished during method 2. The start of each block during method 2 included an amplifier rotation, additional wait time and a baseline measurement. Integration times were 1.049 seconds with a 3 second idle for methods 1 and 3, and 4.194 seconds with a 10 second idle for method 2. One complete analysis involving all three methods and an additional background washout could be completed within approximately 30 minutes. To maximize accuracy and precision, this measurement strategy incorporates a broadly equivalent duration spent measuring defocused electronic baselines as it did measuring half-mass and on-mass intensities.

S4.3. Spike Subtraction, Mass Bias, Abundance Sensitivity, Hydrides and Related Corrections

Spike stripping and mass bias corrections for TIMS and MC-ICPMS data were reduced following the approaches outlined in (12). An exponential mass fractionation law was used to correct both the TIMS and MC-ICPMS uranium analyses (44, 45). For TIMS, mass fractionation is typically $\leq 0.1\% / u$, almost an order of magnitude less than MC-ICPMS and relatively insensitive to the choice of fractionation law used.

Although abundance sensitivity, defined as the ion current of a species at mass m recorded at mass $m-1$ u due to scattered ions, is below 5 ppm on both the TIMS and MC-ICPMS, the large dynamic range of isotope intensities encountered in this study (~ 137.82 for ^{238}U to ^{235}U and ~ 75 for ^{238}U to ^{236}U and ^{233}U) and the required accuracy for $^{238}U/^{235}U$ necessitates detailed consideration of the tail correction. Tail corrections are carefully considered in the literature for $^{234}U/^{238}U$ determinations, where the $^{234}U/^{238}U$ is $\sim 9 \times 10^{-5}$ and we build upon that knowledge (46, 47).

Accurate tail correction requires knowledge of both the tail shape and the magnitude of the abundance sensitivity at the time of analysis, as well as the relative abundance of the isotopes present and the mass differences between them. In multi-isotopic systems, each peak will be affected by each of the other peaks, so that correction for a ‘family of tails’ is required (48). For both the Neptune MC-ICPMS and the Triton TIMS, we have measured the shape of the peak tails extending up-mass and down-mass from a large (ca. 40V ^{238}U) non-spiked CRM 112a using an ion counter. When plotted as $\log(\text{intensity})$ vs. $\log(|238 - \text{mass}|)$, the tails from the ^{238}U ion beam define linear trends (Figure S2), suggesting a power law relationship of the form of equation 1, where a and b are the slope and y-intercept of the linear trend in log-log space, respectively. The up- and down-mass tails define two different trends with separate line parameters, and the up-mass tail has a significantly steeper slope and smaller intercept.

$$\text{intensity} = e^b |238 - \text{mass}|^a \quad (1)$$

In general, the tail parameter (a) is reproducible over multiple analyses on each instrument and is consistent for ^{238}U and ^{235}U ion beams, but differs between the MC-ICPMS and TIMS (Figure S2). The y-intercept (b) is the logarithm of the intensity at mass ($m-1$) and is proportional to the abundance sensitivity, which varies between analyses. Because the power law relationship is scale invariant, once a and b are determined for a single peak, the peak tail for each isotope present can be scaled to its on-peak intensity.

To evaluate tail corrections, baselines for IRMM 3636 ^{233}U - ^{236}U -spiked standard and sample runs were measured at masses 238.54, 237.54, 237.04, 236.54, 235.54, 234.54, 233.54 and 232.54 on the Neptune and 237.04, 236.54, 235.54, 234.54, 233.54 and 232.54 on the Triton (see Tables S2A and B). On the Neptune, intensities at masses 237.54 and 236.54 were used to calculate the down-mass peak tail parameters for ^{238}U for each baseline cycle. The down-mass tails for all other isotopes were then scaled by their measured on-peak intensity and the sum of the down-mass tails were subtracted from all on-peak measurements. The measured intensity at mass 237.04 was displaced above the power law fit through 237.54 and 236.54, likely due to an isobaric interference, as noted in a similar study by Deschamps et al (49) and was therefore ignored. Up-mass tails were corrected using the mean slope and y-intercept of the CRM 112a analyses, measured under identical conditions. For the TIMS determinations we take a similar approach but use 237.04 and 236.54 to define the slope of the tail, assuming that the isobaric interference detected at mass 237.04 on the ICPMS is specifically related to that instrument/ion source.

In order to assess the validity of this combined theoretical and empirical approach to tail correction we also tail-correct the remaining half-mass intensities not used in the slope calculations (i.e., 234.54). The residual half-mass intensities are plotted in Figure S3 and are within uncertainty of the amplifier noise (3 to 5 μV for TIMS and MC-ICPMS).

The observed ion beam intensity at mass 236 on the TIMS is comparable to the expected intensity of the scattered ions down-mass from the ^{238}U beam, whereas the apparent ^{236}U abundance on the Neptune was greater ($^{236}\text{U}/^{238}\text{U}$ of $\sim 3 \times 10^{-7}$) (Figure S2). We speculate that the signal at mass 236 results from ^{235}U hydride as well as residual ^{236}U remaining in the sample introduction system. Following rigorous cleaning of the PFA spray chamber, nebulizer tip and tubing before and after sample runs, a small residual signal at mass 236 remained, illustrating the difficulty of obtaining negligible blanks with an ICPMS sample introduction system. This washout effect should affect both spiked samples and standards equally during analytical

sessions. Because both the sample and the tracer isotopic compositions were nearly identical for each standard and mineral analysis, and the low intensity of the residual ^{236}U (tens of counts per second) compared to the sample ^{236}U (>300 mV), the resulting correction is negligible.

S4.4. Uncertainty Propagation

Our approach to uncertainty propagation and assessment follows from our earlier $^{238}\text{U}/^{235}\text{U}$ study (12). The two levels of uncertainty quoted in this study are: (1) ‘measurement’ uncertainty, or our ability to resolve differences between samples analysed by either analytical platform (TIMS or ICPMS), and (2) ‘total’ uncertainty, which includes systematic uncertainties and is traceable to SI units. The first level comprises measurement repeatability and reproducibility, including signal and amplifier noise during analysis along with the external variance observed for repeated analyses of reference materials (e.g., CRM 112a) on TIMS and ICPMS. The second level additionally includes the systematic uncertainty contribution of the IRMM 3636 tracer used to correct for mass dependent isotopic fractionations. All uncertainties are quoted at the 2σ level.

After propagating all measurement uncertainties, there is resolvable variation in the $^{238}\text{U}/^{235}\text{U}$ values of the zircon samples measured (MSWD = 36 for $n = 44$, excluding Table Cape as an outlier). The measured variability in zircon $^{238}\text{U}/^{235}\text{U}$ reflects the sum of two sources of scatter: the natural $^{238}\text{U}/^{235}\text{U}$ variation and the estimated analytical uncertainties. We assume the distribution of true $^{238}\text{U}/^{235}\text{U}$ zircon values is approximately Gaussian and use an estimate of the overdispersion (28) to calculate the maximum likelihood estimate mean and standard deviation of the underlying $^{238}\text{U}/^{235}\text{U}_{\text{zircon}}$ distribution, 137.818 ± 0.045 . Propagating the additional systematic uncertainty from the IRMM 3636 isotopic composition (16) yields a total uncertainty for $^{238}\text{U}/^{235}\text{U}$ of 137.818 ± 0.050 . However, if IRMM 3636 has also been used to calibrate the tracer used for zircon analysis (e.g., (50)), care must be taken not to ‘double-count’ this systematic uncertainty, and we recommend the measured uncertainty for general use in U-Pb geochronology.

S5. Results

S5.1. Standard Reference Materials Results

The $^{238}\text{U}/^{235}\text{U}$ compositions for a suite of commonly used natural and synthetic reference materials has recently been determined using SI-traceable ^{233}U - ^{236}U double spikes to correct for mass fractionation (12, 51). Included in these studies is the CRM 112a metal assay which has also been reanalyzed by several geochemical laboratories using both TIMS and MC-ICPMS. Agreement was demonstrated between the NIGL TIMS lab and others facilities at the ~50 ppm level (51). To monitor and quantify the internal and external reproducibility of our $^{238}\text{U}/^{235}\text{U}$ and $^{234}\text{U}/^{235}\text{U}$ determinations, and to gauge our experimental accuracy we have routinely analysed the 112a and Harwell uraninite (HU-1) reference materials bracketing our unknowns over several months (Figures S4 and S5; Table S3). Our 112a and HU-1 determinations for $^{238}\text{U}/^{235}\text{U}$ made with both TIMS and ICPMS show agreement with the results published by Condon et al. (12) and the Richter et al. (51) compilation (Figure S6). Consideration here should be made for the slight differences in experimental designs inherent to each study e.g., instrumental and analytical configurations, tailing corrections etc. Significantly, the average $^{234}\text{U}/^{235}\text{U}$ determined for HU-1 by TIMS (0.007554) and ICPMS (0.007563) agrees within 2σ uncertainties with the secular equilibrium $^{234}\text{U}/^{235}\text{U}$ (0.007568 ± 13) defined by Cheng et al. (52) indicating a high level of accuracy in our measurements. $^{234}\text{U}/^{235}\text{U}$ is highly sensitive to tail correction procedures and in-part validates our approach to tail corrections.

S5.2. Mineral $^{234}\text{U}/^{235}\text{U}$ Results

Thirty-five of the 45 zircons have measured $^{234}\text{U}/^{235}\text{U}$ values that overlap at 2σ with the secular equilibrium values determined by Cheng et al. (52), with notable exceptions being Paleoproterozoic rapakivi metadiorite 194720 and Triassic volcanic ash layer JP9733 (Figure S7 and Table S4). Neither sample has an anomalous $^{238}\text{U}/^{235}\text{U}$ and no obvious reason for their anomalously low $^{234}\text{U}/^{235}\text{U}$ values has been identified. We tentatively ascribe low $^{234}\text{U}/^{235}\text{U}$ to preferential leaching of ^{234}U in situ, or during sample pre-treatment steps. Similarly, ^{234}U leaching effects may be subtly expressed in the eight other samples with $^{234}\text{U}/^{235}\text{U}$ slightly below secular equilibrium. Davis and Krogh (53) have previously attributed low zircon $^{234}\text{U}/^{238}\text{U}$ values to preferential dissolution of ^{234}U from alpha-recoil damaged lattice sites during acid leaching. Twelve of the thirteen other mineral samples also recorded $^{234}\text{U}/^{235}\text{U}$ values that overlap within their 2σ uncertainties with secular equilibrium, including both titanite samples and five of six monazite samples. The low precision of our $^{234}\text{U}/^{235}\text{U}$ is due to the small ^{234}U signals (~ 1 to 2 mV) and is insufficient to assess $\lambda^{234}\text{U}/\lambda^{238}\text{U}$ (52), but we consider our $^{234}\text{U}/^{235}\text{U}$ values to be accurate at the stated level based upon our analyses of CRM 112a and HU-1.

S5.3. Leachate Results

The chemical abrasion technique (42), applied to all zircons analyzed here and described in Section S2, preferentially removes radiation-damaged zones of zircon that may have behaved as open systems, as well as mineral and/or melt inclusions. The leachates from 26 zircon and one titanite sample were analysed for U concentration. Of those, 18 leachates (typically with higher U concentrations) were selected for a high-precision $^{238}\text{U}/^{235}\text{U}$ determination, and were analysed using the same chemical and mass-spectrometry procedures outlined above for the zircon residues. The U isotope data for the leachate analyses are presented in Figure S8 and Table S5. Each of the 17 zircon leachates exhibit systematically lower $^{238}\text{U}/^{235}\text{U}$ compared to the zircon residue, with an average offset of 88 ppm. This implies preferential leaching of ^{235}U from the crystal lattice and/or preferential dissolution of zircon and/or mineral inclusions with lower $^{238}\text{U}/^{235}\text{U}$. The systematic difference between the leachate and residue suggests preferential leaching of ^{235}U from the crystal lattice as a viable mechanism.

Using the residue $^{238}\text{U}/^{235}\text{U}$ to determine a Pb-Pb zircon date assumes that the U and Pb remain coupled during the chemical abrasion procedure, so that the measured uranium isotopic composition of the residue is responsible for ingrowth of the measured radiogenic Pb isotopic composition. The bulk $^{238}\text{U}/^{235}\text{U}$ is generally within the 2σ analytical uncertainty of the residue. Thus if this assumption is not accurate we do not expect it to significantly affect our conclusions.

SOM Text

S6. Impact on accuracy of $^{207}\text{Pb}/^{235}\text{U}$ and $^{206}\text{Pb}/^{238}\text{U}$ dates

It is not possible to precisely measure the $^{238}\text{U}/^{235}\text{U}$ for most modern geochronological applications because small sample sizes and the low relative abundance of ^{235}U limit the achievable precision. Instead, the quantity of ^{235}U used to calculate the $^{207}\text{Pb}/^{235}\text{U}$ date is commonly derived by dividing the measured moles of ^{238}U by the assumed $^{238}\text{U}/^{235}\text{U} = 137.88$. This assumption is required when either a ^{235}U tracer is employed during isotope dilution and/or when the $^{238}\text{U}/^{235}\text{U}$ ratio cannot be determined with the required precision, which is true for almost all routine mineral U-Pb dating studies. Similarly, for microbeam U-Pb applications it is routine to only measure ^{238}U and use an assumed $^{238}\text{U}/^{235}\text{U}$ ratio to determine the abundance of ^{235}U or vice versa. For isotope dilution studies that employ a mixed ^{233}U - ^{235}U double tracer, an

assumed $^{238}\text{U}/^{235}\text{U}_{\text{sample}}$ ratio is used to calculate the relative ^{235}U contributions from the tracer and sample in order to quantify mass dependent fractionation, which will impact the calculated moles of ^{238}U and hence the $^{238}\text{U}/^{206}\text{Pb}$ date. Thus $^{206}\text{Pb}/^{238}\text{U}$, $^{207}\text{Pb}/^{235}\text{U}$, and $^{207}\text{Pb}/^{206}\text{Pb}$ dates all rely on the $^{238}\text{U}/^{235}\text{U}$ ratio in different ways.

Given that there are numerous configurations of sample/tracer and $\text{U}/\text{Pb}_{\text{tracer}}$ ratios possible, we have chosen to explore the impact of $^{238}\text{U}/^{235}\text{U}$ on $^{235}\text{U}/^{207}\text{Pb}$ and $^{238}\text{U}/^{206}\text{Pb}$ dates with data calculated using a hypothetical ^{205}Pb - ^{233}U - ^{235}U tracer with a U/Pb ratio fixed at 100, a range of sample/tracer ratios ($^{206}\text{Pb}_{\text{sample}}/^{205}\text{Pb}_{\text{tracer}}$ from 0.0001 to 20) to quantify the difference in dates between using $^{238}\text{U}/^{235}\text{U} = 137.88$ ('consensus value') and $^{238}\text{U}/^{235}\text{U} = 137.818 \pm 0.045$ (average $^{238}\text{U}/^{235}\text{U}_{\text{zircon}}$, this study). Figure S9 illustrates the results of these calculations (using the algorithm of McLean et al. (54)) for a number of test ages (50 Ma, 100 Ma, 500 Ma, 1 Ga, 2 Ga and 4.4 Ga) for the range of parameters described above. Plots S9A and S9B show that for $^{206}\text{Pb}/^{238}\text{U}$ dates there is a strong dependence on the sample/tracer ratio, with differences in $^{238}\text{U}/^{235}\text{U}$ resulting in increasing inaccuracy as the sample/tracer ratio increases, and for a given sample/tracer ratio the percentage date difference increases as a function of sample age. Importantly, for samples with typical sample/tracer ratios ($^{206}\text{Pb}/^{205}\text{Pb} < 5$) the difference for a 50 Ma sample (the most sensitive of our test ages) is less than 2 kyr, and although the difference increases as sample age decreases, the sample/tracer ratio typically decreases, mitigating the impact of $^{238}\text{U}/^{235}\text{U}$ inaccuracies on $^{206}\text{Pb}/^{238}\text{U}$ dates. For $^{207}\text{Pb}/^{235}\text{U}$ dates, the impact is intermediate between the impact on $^{207}\text{Pb}/^{206}\text{Pb}$ dates and $^{206}\text{Pb}/^{238}\text{U}$ dates. As with $^{207}\text{Pb}/^{206}\text{Pb}$ dates, there is a strong age dependence on the impact of $^{238}\text{U}/^{235}\text{U}$ on $^{207}\text{Pb}/^{235}\text{U}$ dates even when sample/tracer ratios are optimized (Figure S9C and S9D). However, the magnitude of the difference depends on the sample/tracer ratio, and under-spiked samples exhibit a greater difference between $^{207}\text{Pb}/^{235}\text{U}$ dates calculated using $^{238}\text{U}/^{235}\text{U} = 137.88$ and $^{238}\text{U}/^{235}\text{U} = 137.818$. These model data illustrate that the impact of $^{238}\text{U}/^{235}\text{U}$ on $^{206}\text{Pb}/^{238}\text{U}$ and $^{207}\text{Pb}/^{235}\text{U}$ dates varies as a function of sample age and sample/tracer ratio.

S7. Natural $^{238}\text{U}/^{235}\text{U}$ variation

In order to directly compare the absolute $^{238}\text{U}/^{235}\text{U}$ determinations made on U-bearing minerals in this study with $^{238}\text{U}/^{235}\text{U}$ determinations made on other geological and meteoritic materials, we have reviewed literature data and compiled a dataset of absolute $^{238}\text{U}/^{235}\text{U}$ determinations (Figure 3; Table S6). The majority of these studies attempted to assess variation in $^{238}\text{U}/^{235}\text{U}$, presenting data relative to a standard reference material, and therefore do not present absolute $^{238}\text{U}/^{235}\text{U}$ values. We have normalized these relative $^{238}\text{U}/^{235}\text{U}$ determinations using recently determined absolute values for the standard reference material used (12, 51) (see footnotes for Table S6 for details), allowing us to directly confederate these disparate datasets and assess absolute $^{238}\text{U}/^{235}\text{U}$ values and variation for different geologic reservoirs. Comparison of $^{238}\text{U}/^{235}\text{U}$ determinations made in different laboratories on the same (e.g., CRM 112a (51)) or similar (e.g., seawater (17, 18)) samples indicate data can be compared at the <100 ppm level.

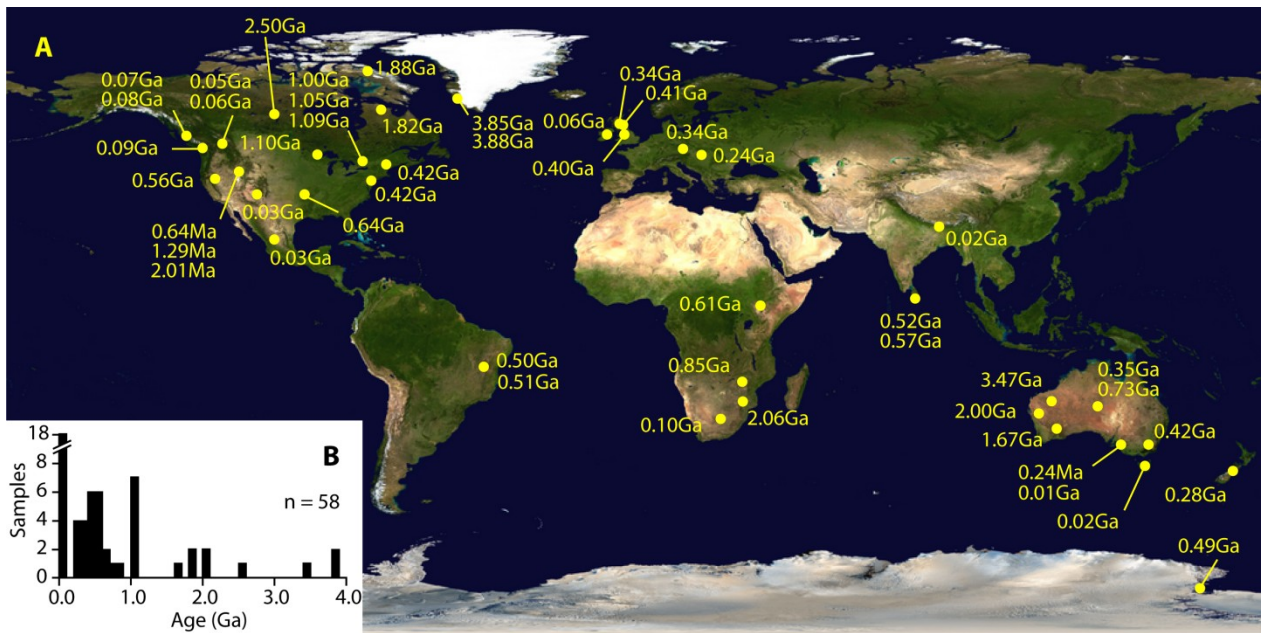


Fig. S1.

(A) Map and (B) histogram indicating the broad distribution of sample locations and ages. Image courtesy of Visible Earth, NASA.

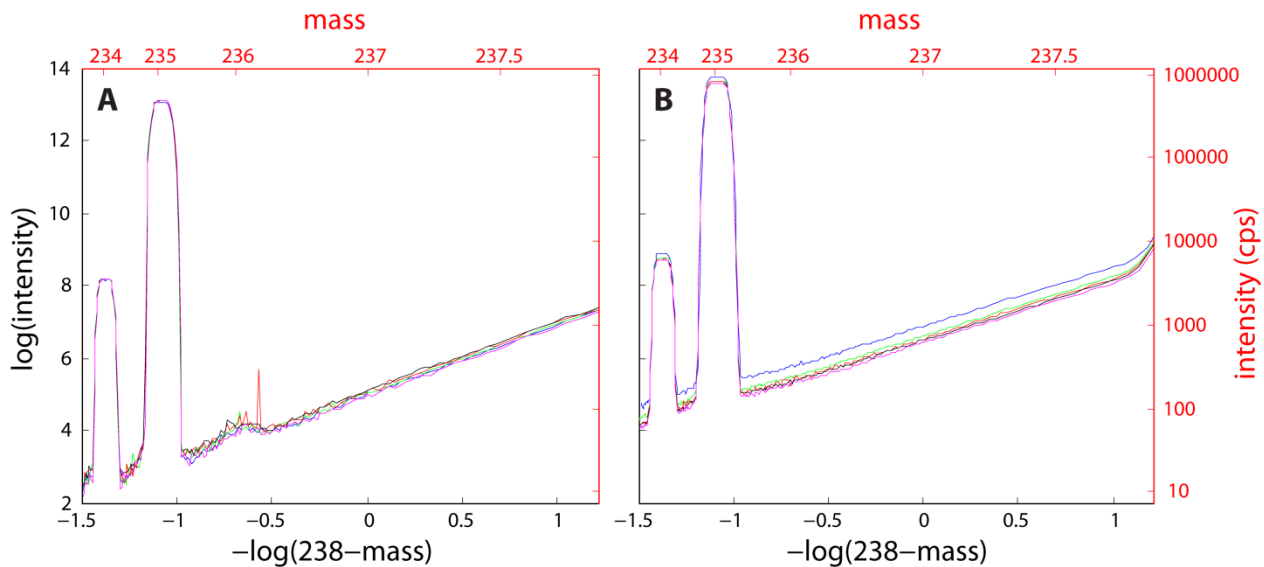


Fig. S2

Mass spectrum from ^{234}U up to ^{238}U using an ion counter on (A) the Neptune ICPMS and (B) Triton TIMS instruments. Five scans are plotted as $\log(\text{intensity})$ vs. $-\log(238-\text{mass})$, given by the black axes, with the mass and intensity equivalents given on the red axes. The linear trend from mass 236.5 past 237.5 implies a power law relationship between down-mass scattered ions and distance (in u) from the peak.

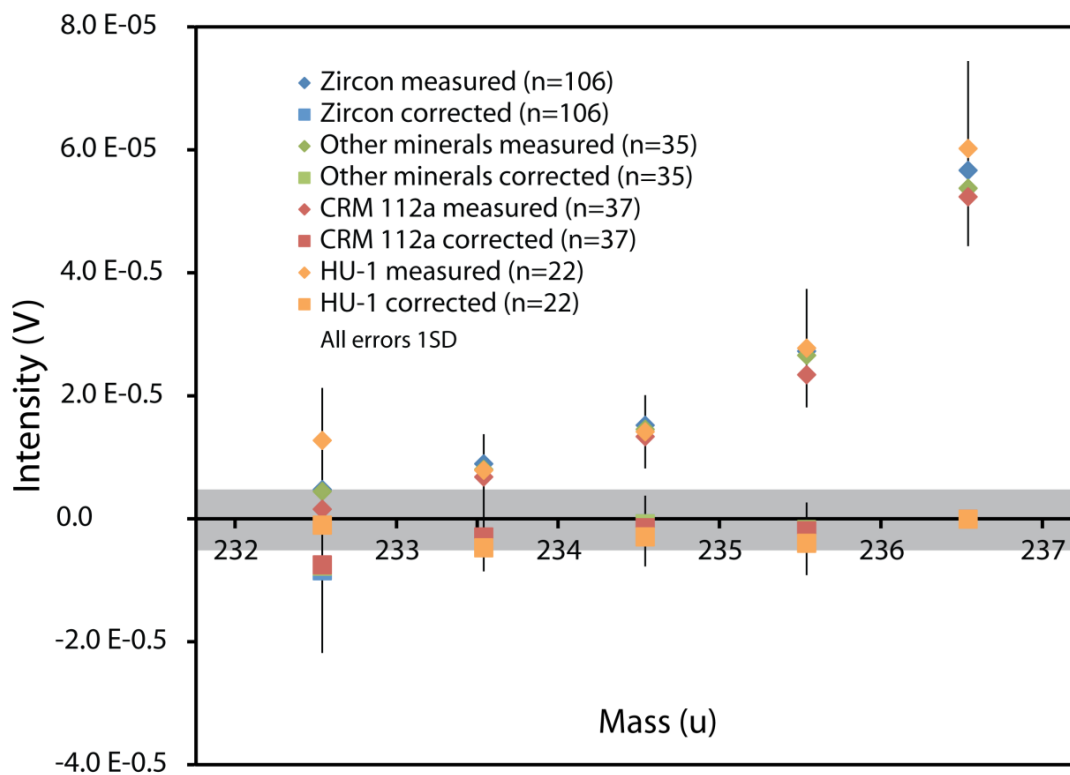


Fig. S3

Tail shape and correction efficiency for Triton TIMS and Neptune MC-ICPMS analyses. Plot of average measured and corrected half-mass intensities made before and after on-peak measurements for zircon, other minerals, CRM 112a and HU-1. Corrected intensities typically lie within the noise of detector baselines (grey band).

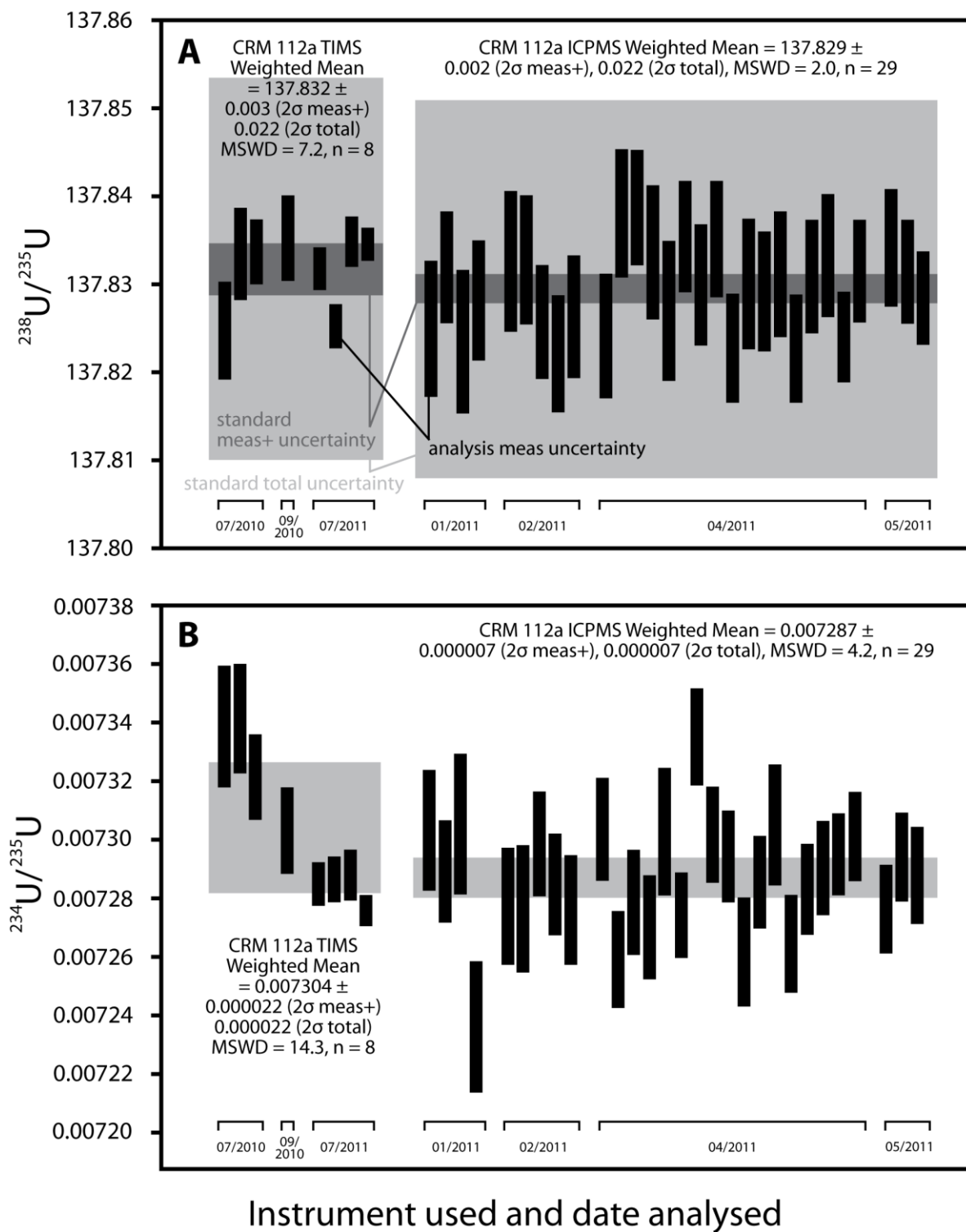
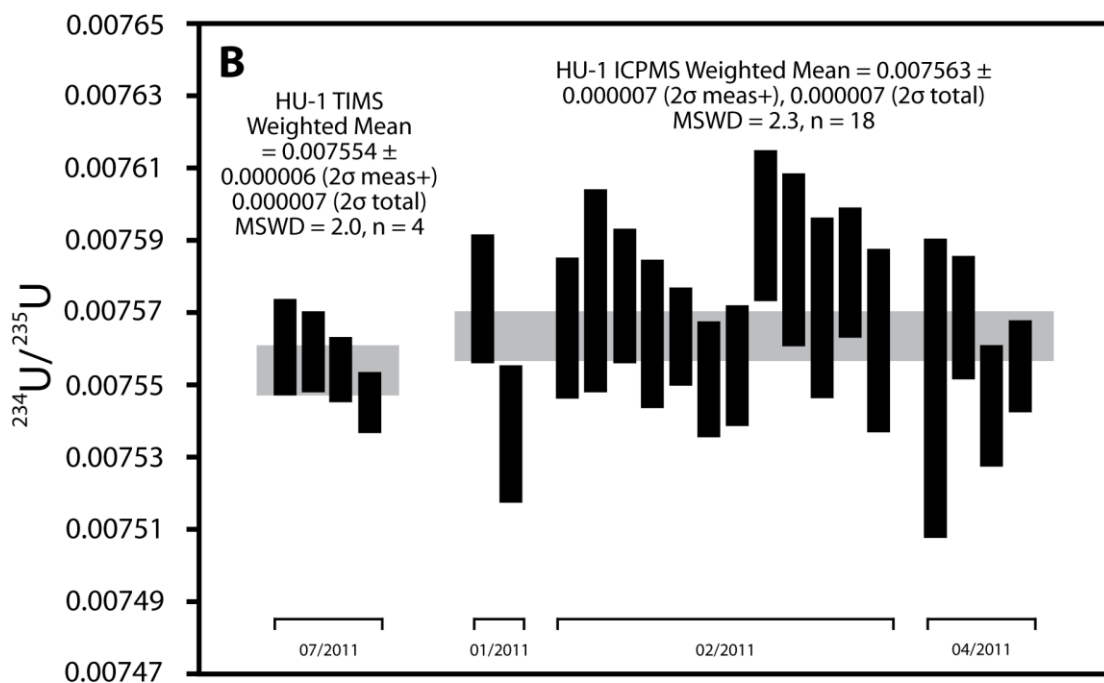
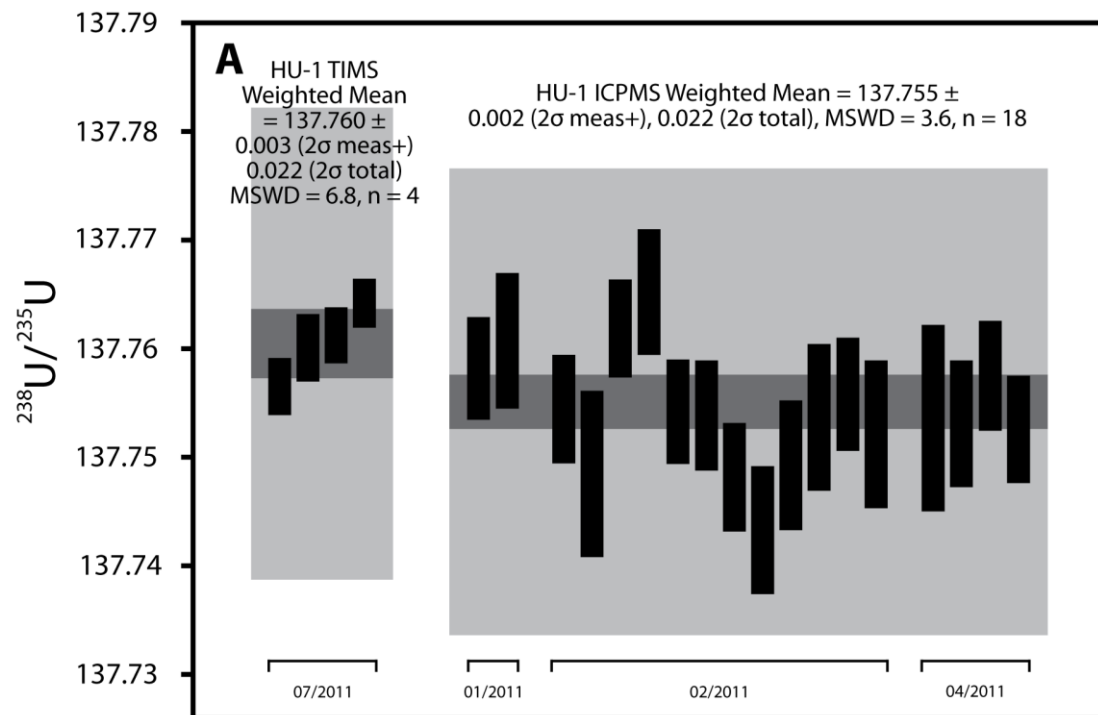


Fig. S4

(A) $^{238}\text{U}/^{235}\text{U}$ and (B) $^{234}\text{U}/^{235}\text{U}$ data for CRM 112a reference solution made by TIMS and MC-ICPMS in this study. Grey bars for (B) are 2σ total uncertainty.



Instrument used and date analysed

Fig. S5

(A) $^{238}\text{U}/^{235}\text{U}$ and (B) $^{234}\text{U}/^{235}\text{U}$ data for HU-1 reference solution made by TIMS and MC-ICPMS in this study. Uncertainty bands same as Figure S4.

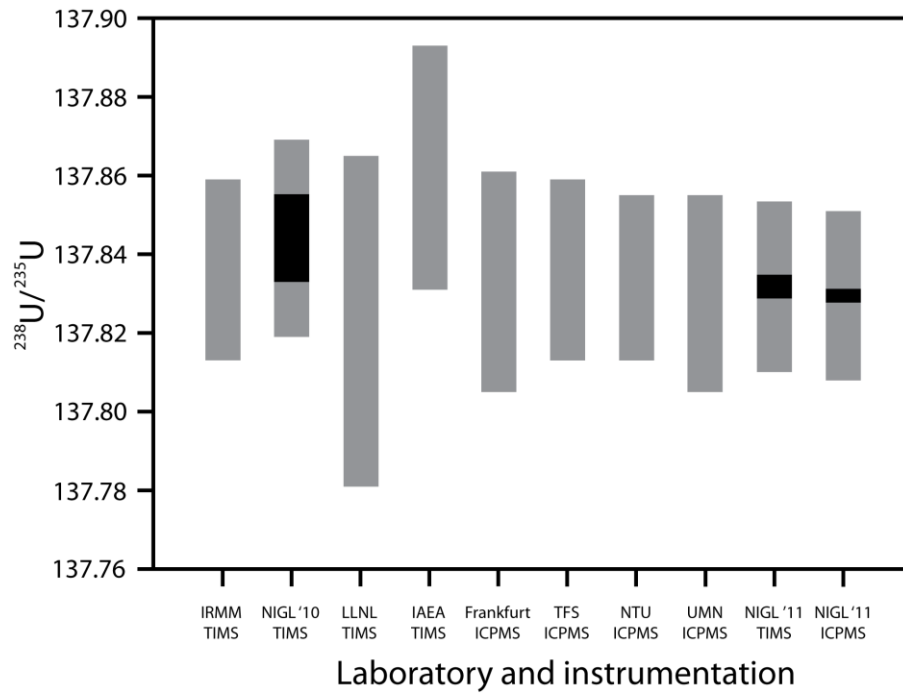


Fig. S6

Compilation of $^{238}\text{U}/^{235}\text{U}$ data for CRM 112a reference solution made by several TIMS and MC-ICPMS labs in this study and published by Richter et al. (2010). Grey bars represent total uncertainty, black bars represent measured uncertainty where published.

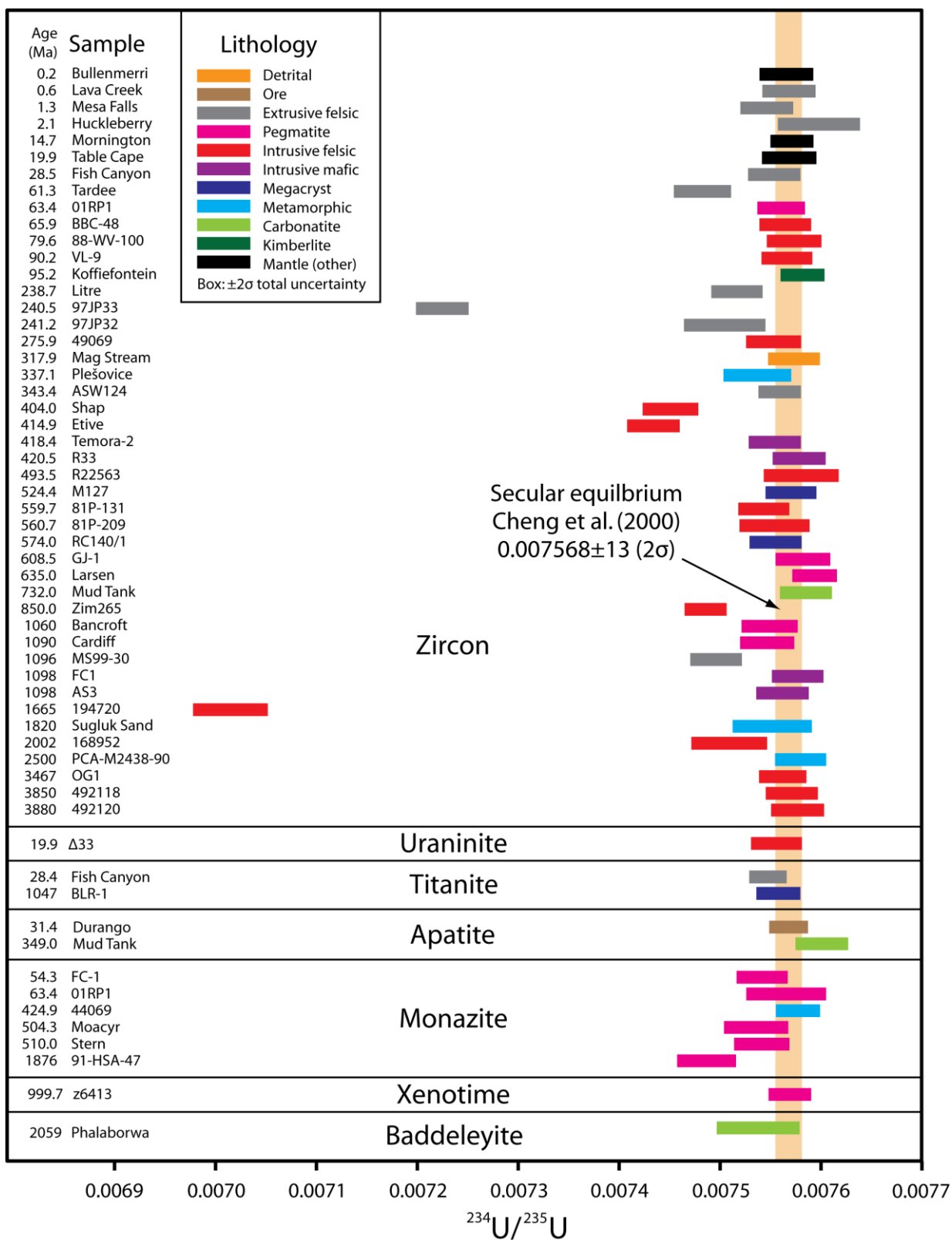


Fig. S7

Plot of $^{234}\text{U}/^{235}\text{U}$ data for U-bearing minerals analysed in this study.

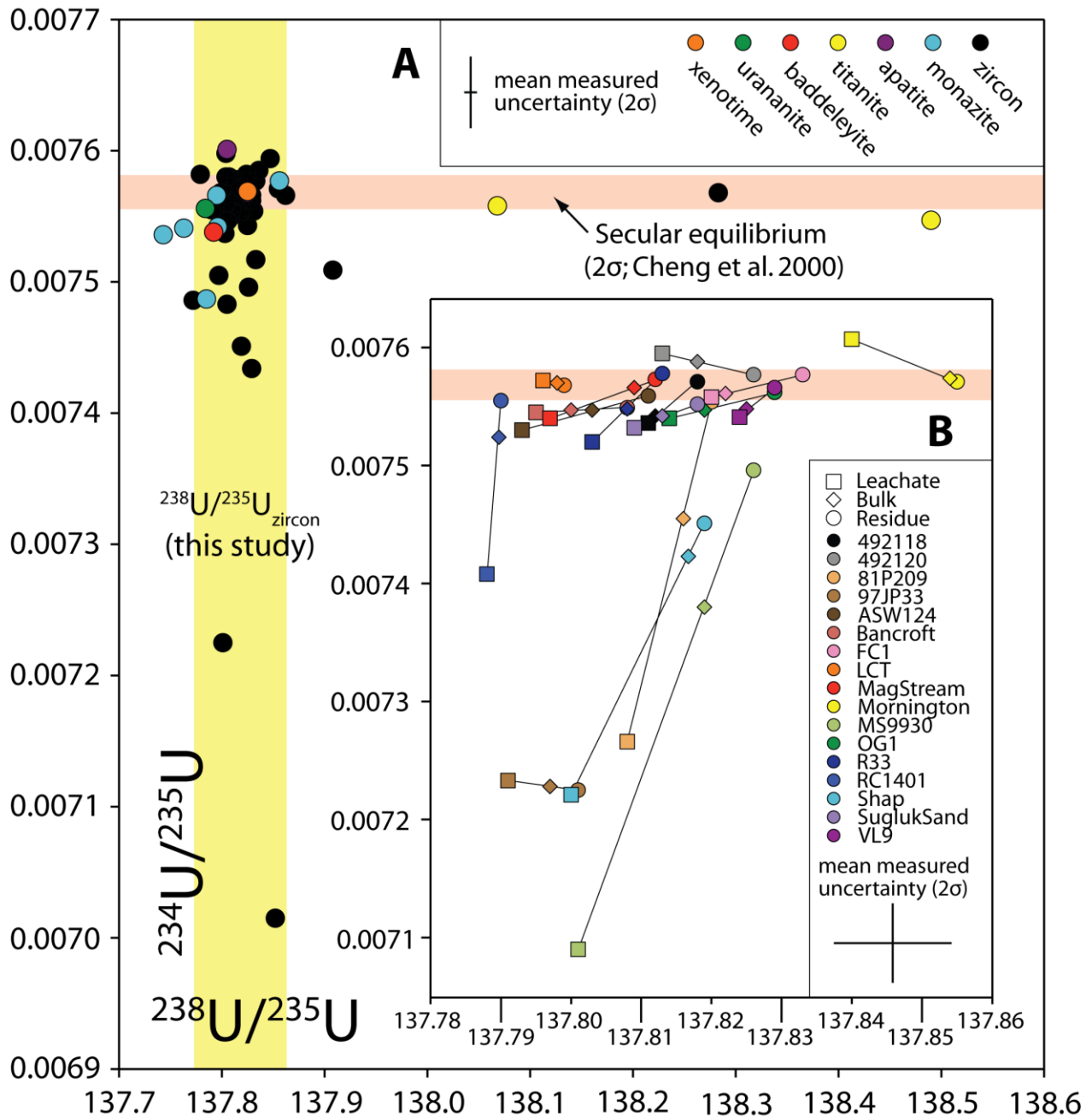


Fig. S8

(A) Cross plot of $^{234}\text{U}/^{235}\text{U}$ and $^{238}\text{U}/^{235}\text{U}$ values for zircons and other U-bearing minerals. For the non-zircon dataset, $^{234}\text{U}/^{235}\text{U}$ is largely invariant and typically overlaps with the secular equilibrium value. There is no clear correlation between $^{234}\text{U}/^{235}\text{U}$ and $^{238}\text{U}/^{235}\text{U}$ in any of the mineral populations. (B) Data from zircon leachate-residue-pairs showing the direction of change in the isotopic composition of the uranium as a result of HF acid leaching. Estimated bulk compositions are based on the proportion of U contained in either reservoir.

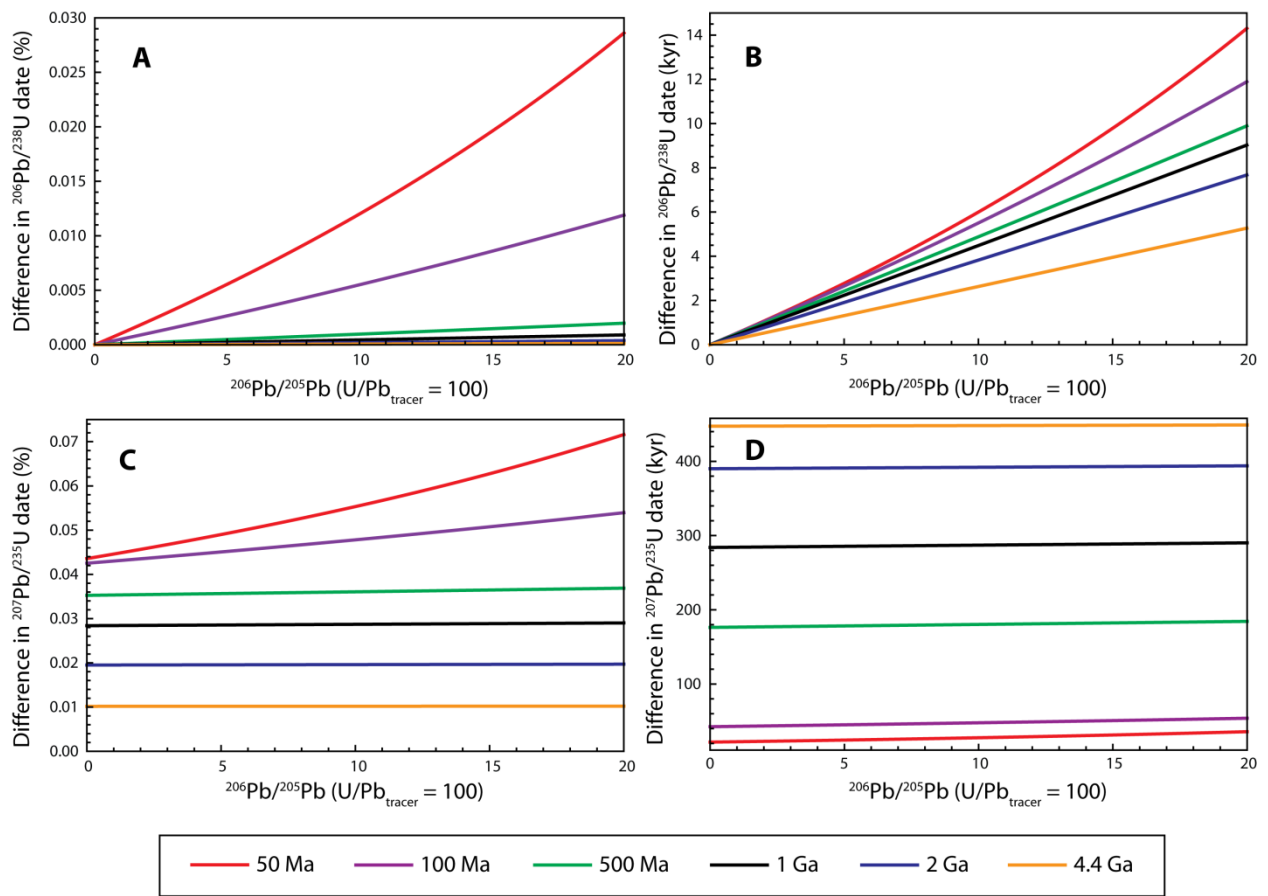


Fig. S9

(A) Plot of percentage difference in $^{206}\text{Pb}/^{238}\text{U}$ dates calculated using $^{238}\text{U}/^{235}\text{U} = 137.88$ and $^{238}\text{U}/^{235}\text{U} = 137.818$ for a range of test ages (50 Ma, 100 Ma, 500 Ma, 1Ga, 2Ga and 4.4 Ga) and for a range of (sample ^{206}Pb)/(tracer ^{205}Pb) ratios, (B) same as A, plotted as absolute difference, (C) same as plot A except for $^{207}\text{Pb}/^{235}\text{U}$ dates; (D) as for plot C, plotted as absolute difference.

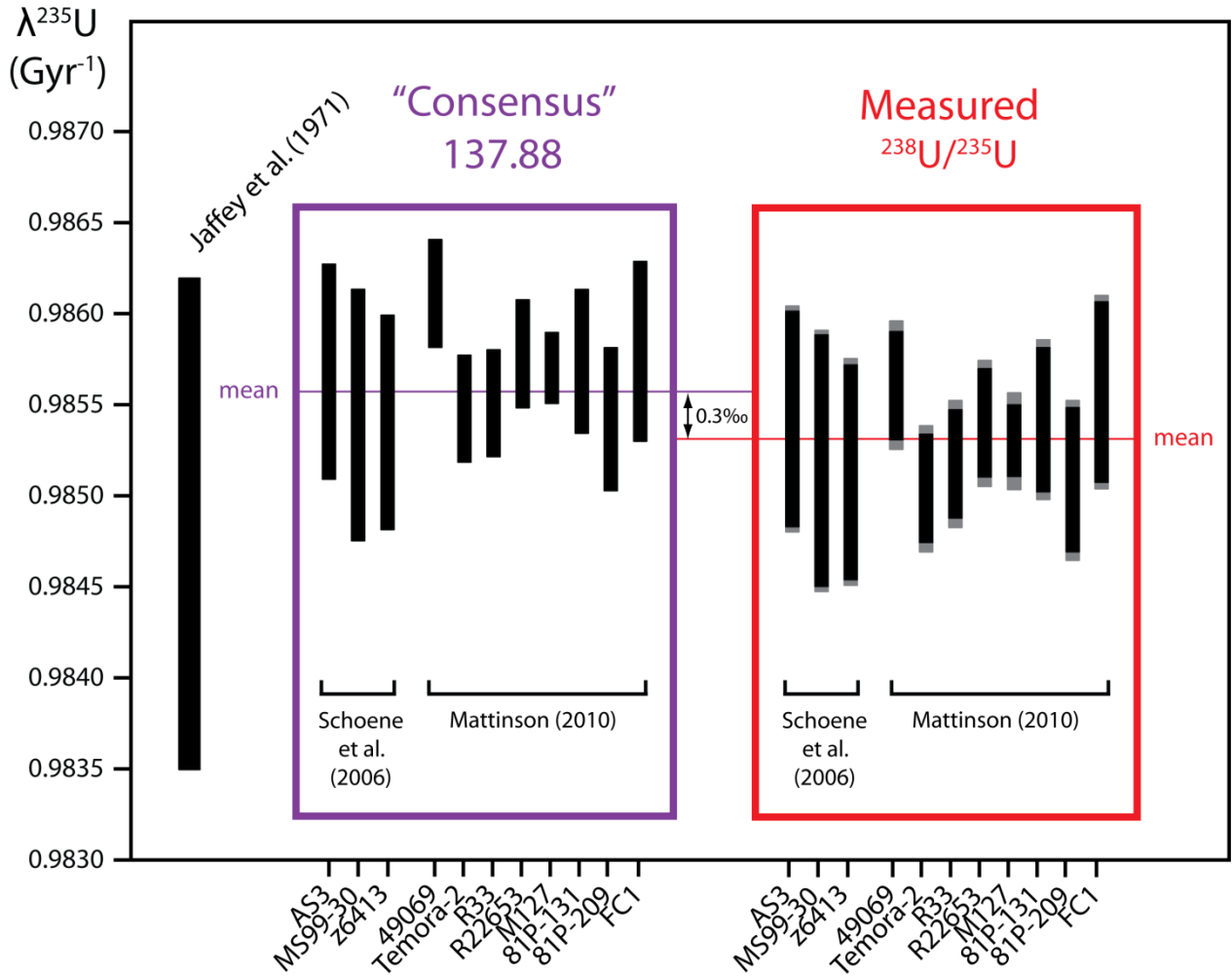


Fig. S10

Re-calculating $\lambda^{235}\text{U}$ against the $\lambda^{238}\text{U}$ of Jaffey et al. (1) using $^{238}\text{U}/^{235}\text{U}$ and high precision U-Pb measurements for closed system zircons decreases $\lambda^{235}\text{U}$ of Mattinson (2) and Schoene et al. (3) by 0.3‰. We urge caution in abandoning the $\lambda^{235}\text{U}$ Jaffey et al. determination (1), and refrain from suggesting a revised $\lambda^{235}\text{U}$ value and uncertainty until a fully traceable ^{238}U - ^{235}U - ^{207}Pb - ^{206}Pb dataset has been generated and evaluated.

Table S1.

Summary of information, age, location and rock type for the U-bearing mineral samples utilized in this study.

Name	Mineral	Lithology	Location	Age estimate	Mineral dated, Decay scheme, Analytical Method	Refs.
Bullenmerri	zircon	most likely mantle-derived	Lake Bullenmerri, Victoria, Australia	0.24±0.04 Ma	Zircon, U-Pb, LA-ICPMS	(55)
LCT (Lava Creek Tuff)	zircon	ash-flow tuff	Yellowstone Volcanic Field, Wyoming, USA	0.639±0.002 Ma	Sanidine, ⁴⁰ Ar/ ³⁹ Ar, total-fusion, plateau and isochron	(56)
MFT (Mesa Falls Tuff)	zircon	ash-flow tuff	Yellowstone Volcanic Field, Idaho, USA	1.285±0.004 Ma	Sanidine, ⁴⁰ Ar/ ³⁹ Ar, total-fusion, plateau and isochron	(56)
HRT (Huckleberry Ridge Tuff)	zircon	ash-flow tuff	Yellowstone Volcanic Field, Idaho, USA	2.059±0.004 Ma	Sanidine, ⁴⁰ Ar/ ³⁹ Ar, total-fusion, plateau and isochron	(56)
Mornington	zircon	most likely mantle-derived	Mornington, Victoria, Australia	14.7±0.5 Ma	Zircon, U-Pb, LA-ICPMS	(55)
Table Cape	zircon	most likely mantle-derived	Table Cape, Tasmania, Australia	19.9±0.5 Ma	Zircon, U-Pb, LA-ICPMS	(55)
Δ33	uraninite	leucogranite	Everest area, southern Tibet	19.93±0.17 Ma	Uraninite, U-Pb, ID-TIMS	(57)
FCT (Fish Canyon Tuff)	titanite	ash-flow tuff	San Juan Mountains, Colorado, USA	28.395±0.078 Ma	Titanite, U-Pb, ID-TIMS	(58)
FCT (Fish Canyon Tuff)	zircon	ash-flow tuff	San Juan Mountains, Colorado, USA	28.476±0.064 Ma	Zircon, U-Pb, ID-TIMS	(58)
Durango	apatite	iron oxide deposit	Chupaderos caldera complex, Durango, Mexico	31.44±0.18 Ma	Sanidine-anorthoclase, ⁴⁰ Ar/ ³⁹ Ar weighted mean	(59)
FC-1	monazite	pegmatite	Canadian Cordillera, British Columbia, Canada	54.3±1.1 Ma	Monazite, U-Th, ID-TIMS	(60)
Tardee	zircon	rhyolite	Tardee Rhyolite Complex, Northern Ireland	61.32±0.09 Ma	Zircon, U-Pb, ID-TIMS	(61)
01RP1	monazite	pegmatite	Canadian Cordillera, British Columbia, Canada	63.4±0.3 Ma	Monazite, U-Pb, ID-TIMS	(62)
01RP1	zircon	pegmatite	Canadian Cordillera, British Columbia, Canada	63.4±0.3 Ma	Zircon, U-Pb, ID-TIMS	(62)
BBC-48	zircon	granite	Bella-Bella Coola area, British Columbia, Canada	65.9±2.0 Ma	Zircon, U-Pb, LA-ICPMS	(55)

88-WV-100	zircon	granite	Kemano-Powell Peak area, British Columbia, Canada	79.6±2.0 Ma	Zircon, U-Pb, LA-ICPMS	(55)
VL-9	zircon	granite	Vancouver-Lillooet area, British Columbia, Canada	90.2±3.0 Ma	Zircon, U-Pb, LA-ICPMS	(55)
Koffiefontein	zircon	kimberlite	Koffiefontein, South Africa	95.2±3.0 Ma	Zircon, U-Pb, LA-ICPMS	(55)
Litre	zircon	volcanic tuff	Balaton Highland, Hungary	238.7±0.6 Ma	Zircon, U-Pb, ID-TIMS	(63)
97JP33	zircon	volcanic tuff	Balaton Highland, Hungary	240.5±0.5 Ma	Zircon, U-Pb, ID-TIMS	(63)
97JP32	zircon	volcanic tuff	Balaton Highland, Hungary	241.2±0.4 Ma	Zircon, U-Pb, ID-TIMS	(63)
49069	zircon	ophiolite plagiogranite	Dun Mountain ophiolite belt, New Zealand	275.94±0.14 Ma	Zircon, U-Pb, ID-TIMS	(2)
Mag Stream	zircon	detrital sediment	Undefined	317.9±8.6 Ma (minimum age)	Zircon, U-Pb, LA-ICPMS	(55)
Plešovice	zircon	granulite	Bohemian Massif, Czech Republic	337.13±0.37 Ma	Zircon, U-Pb, ID-TIMS	(64)
ASW124	zircon	trachyandesite	Midland Valley, Scotland	343.4±1.0 Ma	Zircon, U-Pb, ID-TIMS	(65)
Mud Tank	apatite	carbonatite	Harts Range, Northern Territory, Australia	~349 Ma	Biotite, Rb-Sr maximum	(66)
Shap	zircon	granite	Lake District, England	404.4±0.5 Ma	Zircon, U-Pb, ID-TIMS	(55)
Etive	zircon	granodiorite	Grampian Terrane, Scotland	414.9±0.7 Ma	Zircon, U-Pb, ID-TIMS	(67)
Temora-2	zircon	gabbroic diorite	Lachlan fold belt, New South Wales, Australia	418.37±0.14 Ma	Zircon, U-Pb, ID-TIMS	(2)
R33	zircon	monzodiorite	Braintree Complex, Vermont, USA	420.53±0.16 Ma	Zircon, U-Pb, ID-TIMS	(2)
44069	monazite	metapsammitic gneiss	Wilmington Complex, Delaware, USA	424.86±0.50 Ma	Monazite, U-Pb, ID-TIMS	(68)
R22653	zircon	granodiorite	Granite Harbour Intrusive suite, Antarctica	493.52±0.36 Ma	Zircon, U-Pb, ID-TIMS	(2)
Moacyr	monazite	pegmatite	Itambe District, Brazil	504.3±0.2 Ma	Monazite, U-Pb, ID-TIMS	(69)
Stern	monazite	pegmatite	Itambe District, Brazil	~510 Ma	Monazite, U-Pb, ID-TIMS	(55)
M127	zircon	megacryst	Sri Lanka	524.36±0.14 Ma	Zircon, U-Pb, ID-TIMS	(2)
81P-131	zircon	tonalite	Klamath Mountains, California, USA	559.72±0.38 Ma	Zircon, U-Pb, ID-TIMS	(2)
81P-209	zircon	tonalite	Klamath Mountains, California, USA	560.72±0.31 Ma	Zircon, U-Pb, ID-TIMS	(2)
RC140/1	zircon	megacryst	Sri Lanka	574±21 Ma	Zircon, U-Pb, LA-ICPMS	(55)
GJ-1	zircon	pegmatite	East Africa	608.53±0.37 Ma	Zircon, U-Pb, ID-TIMS	(70)
Larsen	zircon	pegmatite	Wichita Mountains, Oklahoma, USA	~635 Ma	Zircon, α -counting and spectrography	(71)
Mud Tank	zircon	carbonatite	Harts Range, Northern Territory, Australia	732±5 Ma	Zircon, U-Pb, ID-TIMS	(72)

Zim265	zircon	peralkaline granite	Basal Rushinga Complex, Zimbabwe	850±20 Ma	Zircon, U-Pb, LA-ICPMS	(55)
z6413	xenotime	pegmatite	Mattawan, Ontario, Canada	999.7±0.3 Ma	Zircon, U-Pb, ID-TIMS	(3)
BLR-1	titanite	metamorphic megacryst	Bear Lake Diggings locality, Ontario, Canada	1047.1± 0.4 Ma	Titanite, U-Pb, ID-TIMS	(73)
Bancroft	zircon	pegmatite	Renfrew Township, Ontario, Canada	1060-1090 Ma	Zircon, U-Pb, ID-TIMS	(74)
Cardiff	zircon	pegmatite	Haliburton County, Ontario, Canada	~1090 Ma	Zircon, Pb-Pb, MS	(75)
MS99-30	zircon	rhyolite	Palisade, Minnesota, USA	1096.1± 0.4 Ma	Zircon, U-Pb, ID-TIMS	(3)
FC1	zircon	anorthosite	Duluth Complex, Minnesota, USA	1098.47± 0.16 Ma	Zircon, U-Pb, ID-TIMS	(2)
AS3	zircon	anorthosite	Duluth Complex, Minnesota, USA	1098.6± 0.3 Ma	Zircon, U-Pb, ID-TIMS	(3)
194720	zircon	rapakivi metadiorite	Albany-Fraser Orogen, Western Australia, Australia	1665±6 Ma	Zircon, U-Pb, SHRIMP	(76)
Sugluk sand	zircon	granulite	Ungava Peninsular, Northern Quebec, Canada	1820-1840 Ma	Zircon, U-Pb, ID-TIMS	(77)
91-HSA-47	monazite	pegmatite	Piling Group, Nunavut, Canada	1876.4 Ma	Monazite, U-Pb, ID-TIMS	(62)
168952	zircon	tonalite	Gascoyne Complex, Western Australia, Australia	2002±5 Ma	Zircon, U-Pb, SHRIMP	(78)
Phalaborwa	baddeleyite	carbonatite	Phalaborwa Complex, South Africa	2059.60±0.35 Ma	Baddeleyite, U-Pb, ID-TIMS	(79)
PCA-M2438-90	zircon	granulite metapelite	Snowbird Tectonic Zone, Saskatchewan, Canada	2500-2600 Ma	Zircon, U-Pb, ID-TIMS	(55)
OG1	zircon	quartz diorite	East Pilbara Terrane, Western Australia, Australia	3467.1±0.6 Ma	Zircon, U-Pb, ID-TIMS	(80)
492118 (G01/35R)	zircon	tonalite	Itsaq Gneiss Complex, Greenland	>3850 Ma	Zircon, U-Pb, SHRIMP	(81)
492120 (G01/36R)	zircon	tonalite	Itsaq Gneiss Complex, Greenland	3880±8 Ma	Zircon, U-Pb, SHRIMP	(82)

Table S2A.

Cup-configuration and integration time parameters for Triton TIMS determinations.

Line	L1	AX	H1	H2	H3	Integration time (s)	Idle time (s)
1	234.54	235.54	236.54			16.77	15
2	232.54	233.54	234.54			16.77	2
3	²³³ U	²³⁴ U	²³⁵ U	237.041	²³⁸ U	16.77	3
4		²³⁵ U	²³⁶ U	²³⁸ U		16.77	3

Table S2B.

Cup-configuration and integration time parameters for Neptune MC-ICPMS determinations.

Method	L3	L2	L1	AX	H1	H2	H3	Integration time (s)	Idle time (s)
1	232.54	233.54	234.54	235.54	236.54	237.54	238.54	1.049	3
2	²³² Th	²³³ U	²³⁴ U	²³⁵ U	²³⁶ U	237.04	²³⁸ U	4.194	10
3	232.54	233.54	234.54	235.54	236.54	237.54	238.54	1.049	3

Table S3.

Summary of all CRM 112a and HU-1 reference material isotopic data.

Analysis	$^{238}\text{U}/^{235}\text{U}$	$\pm 2\text{SE (meas)}$	$^{234}\text{U}/^{235}\text{U}$	$\pm 2\text{SE (meas)}$
TIMS				
CRM112a 5	137.825	0.006	0.007339	0.000021
CRM112a 6	137.833	0.005	0.007341	0.000019
CRM112a 7	137.834	0.004	0.007321	0.000015
CRM112a 8	137.835	0.005	0.007303	0.000015
CRM112a A	137.832	0.002	0.007285	0.000007
CRM112a B	137.825	0.003	0.007286	0.000008
CRM112a C	137.835	0.003	0.007288	0.000009
CRM112a D	137.835	0.002	0.007276	0.000005
Weighted Mean:	137.832		0.007304	
$\pm 2\sigma$ (abs) meas+:	0.003		0.000022	
$\pm 2\sigma$ (abs) total:	0.022		0.000022	
MSWD total:	7.2		14.3	
n:	8		8	
MC-ICPMS				
CRM112a 12	137.825	0.008	0.007303	0.000021
CRM112a 13	137.832	0.006	0.007289	0.000017
CRM112a 14	137.823	0.008	0.007305	0.000024
CRM112a 15	137.828	0.007	0.007236	0.000022
CRM112a 16	137.833	0.008	0.007277	0.000020
CRM112a 17	137.833	0.007	0.007276	0.000022
CRM112a 18	137.826	0.006	0.007299	0.000018
CRM112a 19	137.822	0.007	0.007285	0.000017
CRM112a 20	137.826	0.007	0.007276	0.000019
CRM112a 21	137.824	0.007	0.007303	0.000018
CRM112a 22	137.838	0.007	0.007259	0.000017
CRM112a 23	137.839	0.007	0.007279	0.000018
CRM112a 24	137.834	0.008	0.007270	0.000018
CRM112a 25	137.827	0.008	0.007303	0.000022
CRM112a 26	137.835	0.006	0.007274	0.000015
CRM112a 27	137.830	0.007	0.007335	0.000017
CRM112a 28	137.835	0.007	0.007302	0.000016
CRM112a 29	137.823	0.006	0.007294	0.000016
CRM112a 30	137.830	0.007	0.007262	0.000019
CRM112a 31	137.829	0.007	0.007285	0.000016
CRM112a 32	137.831	0.007	0.007305	0.000021
CRM112a 33	137.823	0.006	0.007264	0.000017
CRM112a 34	137.831	0.006	0.007283	0.000016
CRM112a 35	137.833	0.007	0.007290	0.000016
CRM112a 36	137.824	0.005	0.007295	0.000014
CRM112a 37	137.831	0.006	0.007301	0.000015
CRM112a 38	137.834	0.007	0.007276	0.000015
CRM112a 39	137.831	0.006	0.007294	0.000015
CRM112a 40	137.828	0.005	0.007288	0.000017

Weighted Mean:	137.829		0.007287	
±2σ (abs) meas+:	0.002		0.000007	
±2σ (abs) total:	0.022		0.000007	
MSWD total:	2.0		4.2	
n:	29		29	
TIMS				
HU1 A	137.757	0.003	0.007560	0.000013
HU1 B	137.760	0.003	0.007559	0.000011
HU1 C	137.761	0.003	0.007554	0.000009
HU1 D	137.764	0.002	0.007545	0.000008
Weighted Mean:	137.760		0.007554	
±2σ (abs) meas+:	0.003		0.000006	
±2σ (abs) total:	0.022		0.000007	
MSWD total:	6.8		2.0	
n:	4		4	
MC-ICPMS				
HU 1	137.758	0.005	0.007574	0.000018
HU 2	137.761	0.006	0.007536	0.000019
HU 3	137.754	0.005	0.007565	0.000019
HU 4	137.748	0.008	0.007576	0.000028
HU 5	137.762	0.005	0.007574	0.000018
HU 6	137.765	0.006	0.007564	0.000020
HU 7	137.754	0.005	0.007563	0.000014
HU 8	137.754	0.005	0.007551	0.000016
HU 9	137.748	0.005	0.007555	0.000017
HU 10	137.743	0.006	0.007594	0.000021
HU 11	137.749	0.006	0.007584	0.000024
HU 12	137.754	0.007	0.007571	0.000025
HU 13	137.756	0.005	0.007581	0.000018
HU 14	137.752	0.007	0.007562	0.000025
HU 15	137.754	0.009	0.007549	0.000041
HU 16	137.753	0.006	0.007568	0.000017
HU 17	137.758	0.005	0.007544	0.000017
HU 18	137.753	0.005	0.007555	0.000013
Weighted Mean:	137.755		0.007563	
±2σ (abs) meas+:	0.002		0.000007	
±2σ (abs) total:	0.022		0.000007	
MSWD total:	3.6		2.3	
n:	18		18	

Table S4.

Summary of all mineral isotopic data. For method: T = TIMS analysis, I = MC-ICPMS analysis. Concentrations for zircon relate to residues following leachate extraction. Concentration for other minerals relate to the bulk phase.

Sample Name:	Mineral	Method	<i>n</i>	U conc. (ppm)	²³⁸ U/ ²³⁵ U	±2σ (abs, meas)	±2σ (abs, total)	²³⁴ U/ ²³⁵ U	±2σ (abs, meas)	±2σ (abs, total)
01RP1	zircon	T+I	6	593	137.804	0.004	0.022	0.007560	0.000024	0.000024
168952	zircon	I	1	101	137.908	0.009	0.022	0.007509	0.000037	0.000018
194720	zircon	I	1	40	137.852	0.009	0.022	0.007015	0.000037	0.000017
49069	zircon	I	2	132	137.801	0.006	0.022	0.007553	0.000027	0.000027
492118	zircon	I	2	19	137.818	0.006	0.022	0.007571	0.000026	0.000026
492120	zircon	I	2	27	137.826	0.006	0.022	0.007577	0.000026	0.000026
81P131	zircon	I	2	227	137.825	0.006	0.022	0.007543	0.000025	0.000025
81P209	zircon	T+I	2	113	137.820	0.008	0.023	0.007554	0.000035	0.000035
88WV100	zircon	I	2	150	137.807	0.006	0.022	0.007573	0.000027	0.000027
97JP32	zircon	I	1	176	137.797	0.010	0.023	0.007505	0.000040	0.000024
97JP33	zircon	I	2	50	137.801	0.006	0.022	0.007225	0.000026	0.000026
AS3	zircon	I	2	76	137.825	0.006	0.022	0.007562	0.000026	0.000026
ASW124	zircon	T+I	6	476	137.811	0.004	0.022	0.007559	0.000021	0.000021
Bancroft	zircon	T+I	4	971	137.808	0.005	0.022	0.007549	0.000028	0.000028
BBC48	zircon	I	2	79	137.817	0.006	0.022	0.007565	0.000026	0.000026
Bullenmerri	zircon	I	2	463	137.862	0.005	0.022	0.007566	0.000026	0.000027
Cardiff	zircon	I	2	2492	137.806	0.006	0.022	0.007547	0.000027	0.000027
Etive	zircon	I	2	657	137.829	0.006	0.022	0.007434	0.000026	0.000026
FC1	zircon	I	2	63	137.833	0.006	0.022	0.007577	0.000025	0.000025
FCT	zircon	T+I	3	277	137.831	0.005	0.022	0.007554	0.000026	0.000026
GJ1	zircon	I	3	223	137.824	0.006	0.022	0.007582	0.000027	0.000027
HRT	zircon	I	1	245	137.804	0.009	0.022	0.007598	0.000041	0.000024
Koffiefontein	zircon	I	3	2	137.779	0.007	0.023	0.007582	0.000022	0.000022
Larsen	zircon	I	3	1450	137.847	0.005	0.022	0.007594	0.000022	0.000022

LCT	zircon	I	2	119	137.799	0.006	0.022	0.007568	0.000026	0.000026
Litre	zircon	I	2	15	137.833	0.006	0.022	0.007517	0.000025	0.000025
M127	zircon	I	2	304	137.812	0.006	0.022	0.007570	0.000025	0.000025
MagStream	zircon	I	2	95	137.812	0.006	0.022	0.007573	0.000026	0.000026
MFT	zircon	I	2	140	137.805	0.006	0.022	0.007546	0.000026	0.000026
Mornington	zircon	I	3	43	137.855	0.005	0.022	0.007571	0.000021	0.000021
MS9930	zircon	I	2	45	137.826	0.006	0.022	0.007496	0.000025	0.000026
MudTank	zircon	I	2	16	137.836	0.006	0.022	0.007585	0.000026	0.000026
OG1	zircon	I	3	51	137.829	0.006	0.022	0.007562	0.000023	0.000023
PCA243890	zircon	I	2	55	137.804	0.006	0.022	0.007580	0.000025	0.000025
Plesovice	zircon	T+I	2	537	137.803	0.007	0.022	0.007537	0.000033	0.000034
R22653	zircon	T	3	813	137.807	0.005	0.022	0.007580	0.000037	0.000037
R33	zircon	I	2	104	137.813	0.006	0.022	0.007578	0.000026	0.000026
RC1401	zircon	I	3	478	137.790	0.005	0.022	0.007555	0.000026	0.000026
Shap	zircon	T+I	4	619	137.819	0.005	0.022	0.007451	0.000027	0.000028
SuglukSand	zircon	I	1	118	137.818	0.008	0.022	0.007552	0.000039	0.000022
TableCape	zircon	I	2	16	138.283	0.006	0.022	0.007568	0.000027	0.000027
Tardee	zircon	I	2	342	137.805	0.007	0.023	0.007483	0.000028	0.000028
Temora2	zircon	I	2	102	137.810	0.006	0.022	0.007554	0.000026	0.000026
VL9	zircon	I	2	39	137.829	0.006	0.022	0.007566	0.000025	0.000025
Zim265	zircon	I	3	26	137.772	0.005	0.022	0.007486	0.000021	0.000021
01RP1	monazite	I	1	769	137.795	0.009	0.022	0.007566	0.000039	0.000022
44069	monazite	I	3	763	137.856	0.005	0.022	0.007577	0.000022	0.000022
91HSA47	monazite	I	2	176	137.785	0.008	0.023	0.007487	0.000029	0.000029
FC-1	monazite	I	3	6868	137.796	0.006	0.022	0.007542	0.000025	0.000025
Moacyr	monazite	I	2	65	137.743	0.007	0.023	0.007536	0.000032	0.000032
Stern	monazite	I	2	493	137.763	0.007	0.022	0.007541	0.000027	0.000027
z6413	xenotime	I	3	8382	137.825	0.005	0.022	0.007569	0.000021	0.000021
Durango	apatite	I	4	7	137.825	0.004	0.022	0.007568	0.000019	0.000019
MudTank	apatite	I	2	3	137.805	0.006	0.022	0.007601	0.000026	0.000026
BLR1	titanite	I	3	95	138.068	0.005	0.022	0.007558	0.000022	0.000022

FCT	titanite	I	4	56	138.490	0.004	0.022	0.007547	0.000019	0.000019
Phalaborwa	baddeleyite	I	1	517	137.792	0.009	0.022	0.007538	0.000041	0.000025
$\Delta 33$	urananite	I	5	220960	137.784	0.004	0.022	0.007556	0.000025	0.000025

Table S5.

Leachate U abundance and isotopic data.

Sample ID	Batch	Mineral	U (µg) residue	U (µg) leachate	% of total U in leachate	²³⁸ U/ ²³⁵ U residue	²³⁸ U/ ²³⁵ U bulk	²³⁸ U/ ²³⁵ U leachate	±2σ (abs, meas)	±2σ (abs, total)	²³⁴ U/ ²³⁵ U residue	²³⁴ U/ ²³⁵ U bulk	²³⁴ U/ ²³⁵ U leachate	±2σ (abs, meas)	±2σ (abs, total)
492118	1	zircon	0.71	3.29	82.2	137.818	137.812	137.811	0.012	0.024	0.007571	0.007542	0.007536	0.000036	0.000036
492120	1	zircon	0.96	1.43	59.8	137.826	137.818	137.813	0.009	0.023	0.007577	0.007588	0.007595	0.000038	0.000038
81P209	1+2	zircon	15.60	8.19	34.4	137.820	137.816	137.808	0.008	0.023	0.007554	0.007455	0.007266	0.000038	0.000041
97JP33	1	zircon	5.60	3.89	41.0	137.801	137.797	137.791	0.008	0.023	0.007225	0.007228	0.007233	0.000037	0.000037
ASW 124	1+2	zircon	81.58	56.41	40.9	137.811	137.803	137.793	0.011	0.024	0.007559	0.007547	0.007530	0.000036	0.000036
Bancroft	1+2+3	zircon	214.26	291.35	57.6	137.808	137.800	137.795	0.008	0.023	0.007549	0.007547	0.007545	0.000037	0.000037
FC1	1	zircon	1.09	5.56	83.7	137.833	137.822	137.820	0.008	0.023	0.007577	0.007561	0.007558	0.000038	0.000038
FCT	2	titanite	25.80	2.77	9.7	138.490	138.422	137.796	0.007	0.022	0.007547	0.007541	0.007481	0.000025	0.000026
LCT	1	zircon	4.05	3.81	48.5	137.799	137.798	137.796	0.008	0.023	0.007568	0.007570	0.007572	0.000026	0.000026
Mag stream	1	zircon	43.95	11.40	20.6	137.812	137.809	137.797	0.006	0.022	0.007573	0.007566	0.007540	0.000026	0.000026
Mornington	1	zircon	39.50	3.18	7.5	137.855	137.854	137.840	0.014	0.025	0.007571	0.007574	0.007607	0.000039	0.000039
MS9930	1+2+3	zircon	8.21	3.27	28.5	137.826	137.819	137.801	0.008	0.023	0.007496	0.007380	0.007090	0.000037	0.000037
OG1	1	zircon	4.82	11.12	69.8	137.829	137.819	137.814	0.004	0.022	0.007562	0.007547	0.007540	0.000019	0.000019
R33	1+2	zircon	11.19	12.11	52.0	137.813	137.808	137.803	0.008	0.023	0.007578	0.007548	0.007520	0.000036	0.000036
RC1401	1	zircon	105.89	28.27	21.1	137.790	137.790	137.788	0.009	0.023	0.007555	0.007524	0.007408	0.000037	0.000037
Shap	1+2	zircon	521.35	72.80	12.3	137.819	137.817	137.800	0.009	0.023	0.007451	0.007423	0.007221	0.000037	0.000037
SuglukSand	1	zircon	84.74	87.79	50.9	137.818	137.813	137.809	0.006	0.022	0.007552	0.007542	0.007532	0.000027	0.000027
VL9	1	zircon	5.17	13.88	72.9	137.829	137.825	137.824	0.008	0.023	0.007566	0.007548	0.007541	0.000037	0.000037
49069	1	zircon	1.20	0.23	16.1	137.801	-	-	-	-	0.007553	-	-	-	-
AS3	1	zircon	0.96	5.82	85.8	137.825	-	-	-	-	0.007562	-	-	-	-
Bullenmerri	1	zircon	769.04	23.34	2.9	137.862	-	-	-	-	0.007566	-	-	-	-
FCT	1	zircon	171.06	1.72	1.0	137.831	-	-	-	-	0.007554	-	-	-	-
Koffiefontein	1	zircon	1.43	0.44	23.5	137.779	-	-	-	-	0.007582	-	-	-	-
M127	1	zircon	4.35	0.04	1.0	137.812	-	-	-	-	0.007570	-	-	-	-
MFT	1	zircon	1.18	0.70	37.2	137.805	-	-	-	-	0.007546	-	-	-	-
Mud Tank	1	zircon	1.98	0.07	3.3	137.836	-	-	-	-	0.007585	-	-	-	-
Table Cape	1	zircon	24.42	1.67	6.4	138.283	-	-	-	-	0.007568	-	-	-	-

Table S6.

Compilation of normalized $^{238}\text{U}/^{235}\text{U}$ determinations on geological materials from the published literature. Absolute $^{238}\text{U}/^{235}\text{U}$ values are relative to a given standard reference materials used in a given study (see footnotes for details).

Sample ID	Material	$^{238}\text{U}/^{235}\text{U}$	\pm (2SD)	Reference
B7 (Hawaii)	Seawater	137.774	0.003	(18)
A9 (Hawaii)	Seawater	137.772	0.003	(18)
B10 (Hawaii)	Seawater	137.775	0.014	(18)
C7 (Bermuda)	Seawater	137.771	0.008	(18)
D11 (Bermuda)	Seawater	137.771	0.004	(18)
D12 (Bermuda)	Seawater	137.775	0.007	(18)
Makarov Basin	Seawater	137.768	0.010	(17)
Makarov Basin	Seawater	137.767	0.021	(17)
H-6 North Sea	Seawater	137.750	0.012	(17)
H-6 North Sea	Seawater	137.760	0.010	(17)
Oeno Pacific	Seawater	137.772	0.006	(17)
Henderson Pacific	Seawater	137.760	0.010	(17)
Oeno Pacific	Modern Coral	137.760	0.017	(17)
Siderastrea (a)+	Coral	137.768	0.015	(18)
Siderastrea (b)+	Coral	137.766	0.001	(18)
Porites+	Coral	137.774	0.015	(18)
AC4-7	Fossil coral	137.766	0.012	(17)
U6-11.1	Fossil coral	137.778	0.008	(17)
U6-11.1 rpt	Fossil coral	137.774	0.010	(17)
U6-11.3	Fossil coral	137.777	0.007	(17)
U6-11.3	Fossil coral	137.771	0.010	(17)
NB-D-4	Fossil coral	137.759	0.012	(17)
NB-D-7	Fossil coral	137.741	0.018	(17)
NEB-1C	Fossil coral	137.775	0.014	(17)
Danube	River Water	137.797	0.008	(17)
Danube	River Water	137.801	0.007	(17)
Danube	River Water	137.796	0.007	(17)
JMN-1	Fe–Mn deposit	137.735	0.010	(17)
JMN-2	Fe–Mn deposit	137.750	0.012	(17)
Mn-A1-core+	Manganese nodule	137.745	0.007	(18)
Mn-A1-core (wet)	Manganese nodule	137.744	0.017	(18)
Mn-A1-mid+	Manganese nodule	137.744	0.004	(18)
Mn-A1-rim+	Manganese nodule	137.744	0.015	(18)
Mn-A1-rim (wet)	Manganese nodule	137.745	0.010	(18)
A-1	Manganese crust	137.755	0.008	(18)
P-1	Manganese crust	137.755	0.014	(18)
M-2+	Banded Iron Formation	137.730	0.023	(18)

TS-9+	Banded Iron Formation	137.706	0.011	(18)
Mau-1	Banded Iron Formation	137.789	0.017	(18)
MaMa-1	Banded Iron Formation	137.733	0.019	(18)
ETH	Dolomite Chimney, lagoon	137.716	0.010	(17)
ETH	Dolomite Chimney, lagoon	137.713	0.010	(17)
KOZ (A)	Speleothem	137.890	0.012	(17)
KOZ (A)	Speleothem	137.881	0.011	(17)
KOZ (B)	Speleothem	137.869	0.012	(17)
SPA-43	Speleothem	137.742	0.011	(17)
SPA-44	Speleothem	137.739	0.012	(17)
SPA-45	Speleothem	137.733	0.015	(17)
SPA-46	Speleothem	137.748	0.039	(17)
Argentarola	Speleothem	137.771	0.010	(17)
Argentarola	Speleothem	137.757	0.010	(17)
Argentarola	Speleothem	137.761	0.010	(17)
FAB-LIG	Speleothem	137.795	0.011	(17)
FAB-LIG	Speleothem	137.801	0.012	(17)
1,000	Carbonate, seawater precipitate	137.742	0.032	(41)
880	Carbonate, seawater precipitate	137.741	0.029	(41)
803	Carbonate, seawater precipitate	137.748	0.021	(41)
728	Carbonate, seawater precipitate	137.764	0.023	(41)
673	Carbonate, seawater precipitate	137.733	0.015	(41)
610	Carbonate, seawater precipitate	137.742	0.019	(41)
585	Carbonate, seawater precipitate	137.723	0.036	(41)
523	Carbonate, seawater precipitate	137.761	0.026	(41)
500	Carbonate, seawater precipitate	137.730	0.028	(41)
435	Carbonate, seawater precipitate	137.720	0.017	(41)
422	Carbonate, seawater precipitate	137.733	0.023	(41)
395	Carbonate, seawater precipitate	137.744	0.019	(41)
363	Carbonate, seawater precipitate	137.744	0.019	(41)
310	Carbonate, seawater precipitate	137.731	0.021	(41)
293	Carbonate, seawater precipitate	137.726	0.017	(41)
132	Carbonate, seawater precipitate	137.750	0.017	(41)
125	Carbonate, seawater precipitate	137.749	0.017	(41)
92	Carbonate, seawater precipitate	137.735	0.029	(41)
76	Carbonate, seawater precipitate	137.738	0.023	(41)
51	Carbonate, seawater precipitate	137.741	0.018	(41)
33	Carbonate, seawater precipitate	137.728	0.029	(41)
23	Carbonate, seawater precipitate	137.741	0.018	(41)
15	Carbonate, seawater precipitate	137.721	0.030	(41)
11	Carbonate, seawater precipitate	137.763	0.023	(41)
8	Carbonate, seawater precipitate	137.723	0.018	(41)
3	Carbonate, seawater precipitate	137.766	0.012	(41)
-4	Carbonate, seawater precipitate	137.741	0.011	(41)

-40	Carbonate, seawater precipitate	137.850	0.008	(41)
-65	Carbonate, seawater precipitate	137.796	0.017	(41)
-98	Carbonate, seawater precipitate	137.749	0.004	(41)
-118	Carbonate, seawater precipitate	137.724	0.034	(41)
-160	Carbonate, seawater precipitate	137.779	0.026	(41)
-270	Carbonate, seawater precipitate	137.763	0.023	(41)
-330	Carbonate, seawater precipitate	137.823	0.018	(41)
-370	Carbonate, seawater precipitate	137.767	0.025	(41)
-390	Carbonate, seawater precipitate	137.775	0.026	(41)
-410	Carbonate, seawater precipitate	137.788	0.015	(41)
10-1 (unit-I)	Black shale	137.822	0.017	(18)
21-1 (unit-I)	Black shale	137.826	0.014	(18)
21-2 (unit-I)	Black shale	137.829	0.006	(18)
25-1 (unit-I)	Black shale	137.833	0.003	(18)
43-1 (unit-I)	Black shale	137.836	0.001	(18)
43-2 (unit-I)	Black shale	137.823	0.003	(18)
55-4 (unit-I)	Black shale	137.837	0.004	(18)
BS5 5 cm	Black shale	137.852	0.007	(40)
BS7. 7 cm	Black shale	137.833	0.007	(40)
BS15 15 cm	Black shale	137.848	0.007	(40)
BS17. 17 cm	Black shale	137.851	0.007	(40)
BS20 20 cm	Black shale	137.857	0.007	(40)
BS27. 27 cm	Black shale	137.815	0.007	(40)
BS37. 37 cm	Black shale	137.812	0.007	(40)
55-3 (unit-II)	Black shale	137.888	0.008	(18)
25-2 (unit-II) (a)	Black shale	137.859	0.008	(18)
25-2 (unit-II) (b)	Black shale	137.854	0.001	(18)
BS25 25 cm	Black shale	137.850	0.007	(40)
BS30 30 cm	Black shale	137.870	0.007	(40)
BS40 40 cm	Black shale	137.884	0.007	(40)
BS45 45 cm	Black shale	137.829	0.007	(40)
BS50 50 cm	Black shale	137.847	0.007	(40)
1261A 48 2w 67-68	Black shale	137.822	0.007	(40)
1261A 48 2w 139-140	Black shale	137.808	0.007	(40)
1261A 48 3w 79-80	Black shale	137.833	0.007	(40)
1261A 48 3w 141-142	Black shale	137.797	0.007	(40)
1261A 48 4w 142-143	Black shale	137.846	0.007	(40)
1261A 48 5w 78-79	Black shale	137.819	0.007	(40)
1261A 48 6w 3-4	Black shale	137.810	0.007	(40)
1261A 46 1w 30-31	Shale	137.839	0.007	(40)
1261A 46 1w 90-91	Shale	137.819	0.007	(40)
1261A 46 5w 130-131	Shale	137.851	0.007	(40)
1261A 47 1w 11-12	Shale	137.846	0.007	(40)
1261A 47 2w 141-142	Shale	137.826	0.007	(40)

1261A 47 4w 91-92	Shale	137.855	0.007	(40)
1261A 47 5w 91-92	Shale	137.839	0.007	(40)
1261A 47 6w 81-82	Shale	137.865	0.007	(40)
1261A 48 1w 69-70	Shale	137.825	0.007	(40)
1261A 48 2w 19-20	Shale	137.812	0.007	(40)
1261A 48 6w 32-33	Shale	137.854	0.006	(40)
1261A 49 1w 125-126.5	Shale	137.847	0.006	(40)
1261A 49 2w 60-61.5	Shale	137.826	0.006	(40)
1261A 49 4w 1-2	Shale	137.836	0.006	(40)
1261A 49 5w 55-56	Shale	137.821	0.006	(40)
Sco	Shale	137.793	0.008	(17)
Sco	Shale	137.789	0.010	(17)
92-763+	Kupferschiefer	137.844	0.012	(18)
92-763 (wet),†	Kupferschiefer	137.837	0.006	(18)
92-765+	Kupferschiefer	137.830	0.011	(18)
92-766+	Kupferschiefer	137.819	0.015	(18)
1H1-42 (42)	Suboxic sediment	137.789	0.004	(18)
1H1-122 (122)	Suboxic sediment	137.808	0.004	(18)
1H2-130 (280)	Suboxic sediment	137.781	0.008	(18)
1H3-22 (322)	Suboxic sediment	137.774	0.008	(18)
1H4-90 (540)	Suboxic sediment	137.807	0.007	(18)
1H5-140 (740)	Suboxic sediment	137.782	0.001	(18)
2H3-70 (1195)	Suboxic sediment	137.800	0.019	(18)
2H3-130 (1255)	Suboxic sediment	137.784	0.015	(18)
Sandstone, Czech Rep. Straz Pod Ralskem	Low-temp redox uranium ore	137.848	0.018	(31)
Sandstone, Gabon — Mouana	Low-temp redox uranium ore	137.859	0.018	(31)
Sandstone, Kazakhstan — Kanzhugan	Low-temp redox uranium ore	137.934	0.018	(31)
Sandstone, Kazakhstan — Uvanas	Low-temp redox uranium ore	137.934	0.018	(31)
Sandstone, Niger — Arlit	Low-temp redox uranium ore	137.895	0.018	(31)
Sandstone, Serbia — Rudnik	Low-temp redox uranium ore	137.961	0.018	(31)
Black shale, Sweden — Ranstadt	Low-temp redox uranium ore	137.865	0.018	(31)
Sandstone, USA — El Mesquite	Low-temp redox uranium ore	137.891	0.018	(31)
Sandstone, USA — Everest Black	Low-temp redox uranium ore	137.871	0.018	(31)
Sandstone, USA — Everest Yellow	Low-temp redox uranium ore	137.909	0.018	(31)
Sandstone, USA — Falls City	Low-temp redox uranium ore	137.892	0.018	(31)
Sandstone, USA — Irigary	Low-temp redox uranium ore	137.821	0.018	(31)
Sandstone, USA — Lucky McGill	Low-temp redox uranium ore	137.887	0.018	(31)
Sandstone, USA — Pathfinder	Low-temp redox uranium ore	137.871	0.018	(31)
Sandstone, USA — Petromic	Low-temp redox uranium ore	137.852	0.018	(31)
Sandstone, USA — Shirley Basin	Low-temp redox uranium ore	137.871	0.018	(31)
Sandstone, USA — Susquehan	Low-temp redox uranium ore	137.918	0.018	(31)
QP conglomerate, Canada — Denison	Non-Redox uranium ore	137.855	0.018	(31)
QP conglomerate, Canada — Miliken Lake	Non-Redox uranium ore	137.826	0.018	(31)
QP conglomerate, Canada — Stanleigh	Non-Redox uranium ore	137.823	0.018	(31)

QP conglomerate, Canada — Stanrock	Non-Redox uranium ore	137.831	0.018	(31)
Metamorphic, Australia — Mary Kathleen	High-temp redox uranium ore	137.833	0.018	(31)
Breccia complex, Australia — Olympic Dam	High-temp redox uranium ore	137.845	0.018	(31)
Intrusive, Australia — Radium Hill	High-temp redox uranium ore	137.836	0.018	(31)
Unconformity, Australia — Ranger	High-temp redox uranium ore	137.846	0.018	(31)
Unconformity, Australia — Rum Jungle	High-temp redox uranium ore	137.846	0.018	(31)
Unconformity, Australia — South Alligator	High-temp redox uranium ore	137.826	0.018	(31)
Intrusive, Canada — Dyno	High-temp redox uranium ore	137.843	0.018	(31)
Vein, Canada — El Dorado	High-temp redox uranium ore	137.809	0.018	(31)
Intrusive, Canada — Faraday	High-temp redox uranium ore	137.837	0.018	(31)
Vein, Canada — Gunnar	High-temp redox uranium ore	137.820	0.018	(31)
Unconformity, Canada — Key Lake	High-temp redox uranium ore	137.792	0.018	(31)
Intrusive, Canada — Madawaska	High-temp redox uranium ore	137.847	0.018	(31)
Unconformity, Canada — Rabbit Lake	High-temp redox uranium ore	137.842	0.018	(31)
Vein, Canada — Rayrock	High-temp redox uranium ore	137.849	0.018	(31)
Vein, DR Congo — Shinkolobwe	High-temp redox uranium ore	137.805	0.018	(31)
Intrusive, Namibia — Rössing	High-temp redox uranium ore	137.836	0.018	(31)
Intrusive, South Africa — Palabora	High-temp redox uranium ore	137.865	0.018	(31)
Vein, USA — Dawn	High-temp redox uranium ore	137.817	0.018	(31)
QP conglomerate, Canada — Blind River	High-temp redox uranium ore	137.835	0.018	(31)
C274 Alkali Basalt	Alkali Basalt	137.800	0.010	(32)
C274 Alkali Basalt	Alkali Basalt	137.814	0.012	(32)
C274 Alkali Basalt	Alkali Basalt	137.804	0.011	(32)
C247 Alkali Basalt	Alkali Basalt	137.812	0.012	(32)
C247 Alkali Basalt	Alkali Basalt	137.800	0.017	(32)
C247 Alkali Basalt	Alkali Basalt	137.836	0.015	(32)
C239 Alkali Basalt	Alkali Basalt	137.808	0.017	(32)
C239 Alkali Basalt	Alkali Basalt	137.817	0.012	(32)
C239 Alkali Basalt	Alkali Basalt	137.803	0.018	(32)
C239 Alkali Basalt	Alkali Basalt	137.789	0.014	(32)
C239 Alkali Basalt	Alkali Basalt	137.815	0.017	(32)
C239 Alkali Basalt	Alkali Basalt	137.811	0.012	(32)
C239 Alkali Basalt	Alkali Basalt	137.785	0.015	(32)
C239 Alkali Basalt	Alkali Basalt	137.801	0.017	(32)
C239 Alkali Basalt	Alkali Basalt	137.825	0.021	(32)
C239 Alkali Basalt	Alkali Basalt	137.818	0.022	(32)
BCR-2+	Basalt	137.789	0.010	(18)
BCR-2-01a	Basalt	137.829	0.030	(30)
BCR-2-01b	Basalt	137.810	0.028	(30)
BCR-2-02a	Basalt	137.836	0.043	(30)
BCR-2-02b	Basalt	137.821	0.032	(30)
BCR-2-02c	Basalt	137.831	0.070	(30)
BEN+	Basalt	137.784	0.004	(18)

BHVO-1 (a)	Basalt	137.795	0.008	(18)
BHVO-1 (b)	Basalt	137.789	0.007	(18)
BHVO-2-1	Basalt	137.784	0.147	(30)
BHVO-2-2	Basalt	137.793	0.055	(30)
C235D Lherzolites	Lherzolite	137.814	0.010	(32)
604 DS MORB Glass	MORB Glass	137.817	0.011	(32)
DTS-2b-1	Dunite	137.833	0.081	(30)
DTS-2b-2	Dunite	137.835	0.059	(30)
DTS-2b-3	Dunite	137.824	0.077	(30)
DTS-2b-4	Dunite	137.810	0.071	(30)
JG-1+	Granodiorite	137.775	0.012	(18)
JG-2+	Granite	137.784	0.011	(18)
G-2+	Granite	137.801	0.010	(18)
NIM-G	Granite	137.766	0.008	(18)
Juvinas	Eucrites	137.812	0.012	(32)
Juvinas	Eucrites	137.818	0.014	(32)
Stannern	Eucrites	137.789	0.017	(32)
Stannern	Eucrites	137.806	0.015	(32)
ALHA 78132	Eucrites	137.801	0.019	(32)
Guareña	Ordinary Chondrites	137.818	0.076	(32)
Bruderheim	Ordinary Chondrites	137.801	0.017	(32)
Leedey	Ordinary Chondrites	137.789	0.028	(32)
Leedey	Ordinary Chondrites	137.832	0.039	(32)
Leedey	Ordinary Chondrites	137.800	0.023	(32)
Ausson	Ordinary Chondrites	137.779	0.015	(32)
Ausson	Ordinary Chondrites	137.803	0.021	(32)
Mezö-Madaras	Ordinary Chondrites	137.779	0.015	(32)
AllendeH	Carbonaceous Chondrites	137.841	0.034	(32)
AllendeH	Carbonaceous Chondrites	137.851	0.033	(32)
Allende C	Carbonaceous Chondrites	137.768	0.019	(33)
Allende D	Carbonaceous Chondrites	137.789	0.026	(33)
Allende 1-a	Carbonaceous Chondrites	137.715	0.056	(30)
Allende 1-b	Carbonaceous Chondrites	137.771	0.050	(30)
Allende-1c	Carbonaceous Chondrites	137.739	0.036	(30)
Allende 1-d	Carbonaceous Chondrites	137.769	0.041	(30)
Allende 1-e	Carbonaceous Chondrites	137.758	0.035	(30)
Allende-chondrules	Carbonaceous Chondrites	137.724	0.040	(30)
Allende WR	Carbonaceous Chondrites	137.774	0.012	(25)
Murchison WR	Carbonaceous Chondrites	137.818	0.042	(25)
Murchison C	Carbonaceous Chondrites	137.796	0.032	(33)
Murchison	Carbonaceous Chondrites	137.763	0.034	(32)
Tafassasset	Carbonaceous Chondrites	137.784	0.030	(33)
CAI_SJ-101	Calcium-aluminum rich inclusions	137.876	0.043	(30)
CAI 164	Calcium-aluminum rich inclusions	137.788	0.017	(25)

CAI 165	Calcium-aluminum rich inclusions	137.783	0.011	(25)
CAI 166	Calcium-aluminum rich inclusions	137.358	0.039	(25)
CAI 167	Calcium-aluminum rich inclusions	137.587	0.042	(25)
CAI 168	Calcium-aluminum rich inclusions	137.834	0.009	(25)
CAI 170	Calcium-aluminum rich inclusions	137.859	0.039	(25)
CAI 171	Calcium-aluminum rich inclusions	137.752	0.030	(25)
CAI 172	Calcium-aluminum rich inclusions	137.786	0.039	(25)
CAI 173	Calcium-aluminum rich inclusions	137.745	0.039	(25)
CAI 174	Calcium-aluminum rich inclusions	137.797	0.004	(25)
CAI 175	Calcium-aluminum rich inclusions	137.629	0.030	(25)
CAI 3/4	Calcium-aluminum rich inclusions	137.429	0.020	(25)
CAI 3531-D	Calcium-aluminum rich inclusions	137.565	0.026	(25)
NWA 2976 WR1	Basaltic, ungrouped	137.751	0.018	(39)

1. Data from references (17, 18, 25, 30, 39-41) are normalized to a $^{238}\text{U}/^{235}\text{U}$ value of 137.829 for CRM 112a (CRM 145) and SRM 960 (this study and (12, 51))
2. Data from reference (31) are relative to CRM 129-A and validated using IRMM 184.
3. Data from references (32, 33) are normalized to a $^{238}\text{U}/^{235}\text{U}$ value of 137.829 for CRM 112a (CRM 145) (this study and (12, 51)) via CU-1 standard used in these studies and (17).

Additional Databases S1 to S5 (zipped archives)

Database_S1._TIMSall

Database_S2._MC-ICPMSstds

Database_S3._MC-ICPMSzircon

Database_S4._MC-ICPMSotherminerals.leachates

Database_S5._Compilation

Databases S1 to S4 contain raw and processed data for each analysis collected with TIMS and MC-ICPMS on standards (CRM 112a and HU-1) and mineral samples (zircon, other minerals, leachates). Database S5 contains a compilation of the above material and summary statistics for each sample.